magnetochemistry

MDPI

Article

Titan Yellow and Congo Red Removal with Superparamagnetic Iron-Oxide-Based Nanoparticles Doped with Zinc

Paulina Pietrzyk [1], Nguyen Thu Phuong [2], Sunday Joseph Olusegun [1], Nguyen Hong Nam [3], Dinh Thi Mai Thanh [4], Michael Giersig [5], Paweł Krysiński [1] and Magdalena Osial [5,*]

[1] Faculty of Chemistry, University of Warsaw, Pasteura 1, 02-093 Warsaw, Poland
[2] Institute for Tropical Technology, Vietnam Academy of Science and Technology, 18 Hoang Quoc Viet, Cau Giay, Hanoi 10000, Vietnam
[3] Faculty of Energy, University of Science and Technology of Hanoi, Vietnam Academy of Science and Technology, 18 Hoang Quoc Viet, Cau Giay, Hanoi 10000, Vietnam
[4] University of Science and Technology of Hanoi, Vietnam Academy of Science and Technology, 18 Hoang Quoc Viet, Cau Giay, Hanoi 10000, Vietnam
[5] Department of Theory of Continuous Media and Nanostructures, Institute of Fundamental Technological Research, Polish Academy of Sciences, Pawińskiego 5B, 02-106 Warsaw, Poland
* Correspondence: mosial@ippt.pan.pl; Tel.: +48-22-826-12-81

Abstract: In this work, we present magnetic nanoparticles based on iron oxide doped with zinc synthesized using the wet co-precipitation method for environmental application. The morphology of the samples was revealed by SEM and TEM, which showed particles of granular shape and size of about 15 nm. The specific surface areas of the materials using the BET method were within the range of 85.7 to 101.5 $m^2 g^{-1}$ depending on the zinc content in the superparamagnetic iron oxide nanoparticles (SPIONs). Magnetometry was performed to determine the magnetic properties of the particles, indicating superparamagnetism. Synthesized magnetic nanoparticles with different amounts of zinc dopant were used as an adsorbent to remove model pollutant Titan yellow (TY) from the aqueous solutions. Adsorption was determined by investigating the effects of sorbent amount, dye concentration, and contact time. The synthesized material removed Titan yellow quickly and efficiently within the physical adsorption. The adsorption isotherms were consistent with the models proposed by Langmuir and Redlich-Peterson. The monolayer adsorption capacities were 30 and 43 mg g^{-1} for Fe_3O_4 and Fe_3O_4@10%Zn, respectively, for the removal of TY. However, that of Congo red is 59 mg g^{-1} by Fe_3O_4@10%Zn. The proposed nanoparticles offer fast and cost-effective water purification, and they can be separated from solution using magnets.

Keywords: superparamagnetic particles; pollution treatment; Titan yellow; Congo red; adsorption isotherm; iron oxide

Citation: Pietrzyk, P.; Phuong, N.T.; Olusegun, S.J.; Hong Nam, N.; Thanh, D.T.M.; Giersig, M.; Krysiński, P.; Osial, M. Titan Yellow and Congo Red Removal with Superparamagnetic Iron-Oxide-Based Nanoparticles Doped with Zinc. *Magnetochemistry* **2022**, *8*, 91. https://doi.org/10.3390/magnetochemistry8080091

Academic Editor: Redha Taiar

Received: 18 July 2022
Accepted: 12 August 2022
Published: 14 August 2022

1. Introduction

Water pollution is one of the most demanding environmental challenges. Among many compounds generated by anthropogenic activity are dyes from the textile, paper, tanneries, cosmetic, plastic, and food industries, with the production of 1,000,000 tons globally [1]. Dyes used for colorizing textiles, leathers, and paper are mainly based on synthetic chemicals of aromatic structure, which have adverse effects on the environment. One of the most commonly used groups of dyes is azo-based compounds. Their removal from aquatic reservoirs and wastewater is of great concern, so water purification methods have been developed that propose many materials for use as adsorbents. Activated carbon [2], biochar [3], zeolites [4,5], biosorbents [6], and metal organic frameworks (MOFs) [7,8] have all been investigated and used. Recently, nanomaterials have been proposed as novel adsorbents offering a high volume-to-surface ratio, high adsorption capacity, cost-effective processing,

and feasibility. Different nanomaterials such as functionalized multi-walled carbon nanotubes [9], hydroxyapatite/chitosan composites [10], supported chitosan [11], Au-decorated Bi_2S_3 nanorods [12], etc. have been used for the removal of dyes from wastewater.

Nevertheless, the great effectiveness of magnetic nanomaterials offers the feasibility of pollutant adsorption as well as sorbent removal from water using magnets. In this regard, much attention has been paid to magnetic metal oxides such as $CoFe_2O_4$ [13], $NiFe_2O_4$ [14], magnetic Fe_3O_4/chitosan nanoparticles (MFe_3O_4/CS NPs) and arginine-modified MFe_3O_4/CS nanoparticles [15], magnetic lignosulfonate [16], polyaniline/Fe_3O_4 [17], Fe_3O_4 nanowalls [18], γ-Fe_2O_3 [19], etc. These materials are widely used to treat dyes such as Titan yellow (TY) and Congo red that are released into the environment from industrial and textile effluents. Despite wide application, some studies show a toxicity assay [20–22].

Iron oxide, Fe_3O_4, is a promising candidate for aqueous pollution removal, offering non-cytotoxicity, a high surface-area-to-volume ratio, strong adsorption capacities, and photostability. They can be easily doped with several metals, including zinc [23], for biomedical [24–26] or environmental use such as the removal of phenol and ketoprofen [27], methylene blue dye [28], methyl orange, Congo red [29] and rhodamine B dyes [30], malachite green [31], H_2S [32], Hg(II) ions [33], and Th(IV) ions [34]. Additionally, their magnetic properties can facilitate the removal of nanoparticles with adsorbed pollutants from an aqueous suspension with an external magnet.

In this paper, we present an application of iron-oxide-based nanoparticles doped with zinc for aqueous pollution treatment. The proposed material is environmentally friendly and has a high surface area. Its magnetic properties make it possible to magnetically separate the sorbent after adsorption in a facile way. Nanoparticles prepared using co-precipitation techniques have a high affinity to the adsorption of dye-based pollutants on their surface, and post-treatment, they can be collected on magnets and removed from the solution, leading to high water remediation efficiency. The obtained material has superparamagnetic properties, spherical shape, a size below 20 nm and a developed surface that makes it suitable for aqueous pollution treatment. Titan yellow and Congo red removal via magnetic separation was investigated using UV-vis spectrometry, revealing the potential of this material for environmental studies. Zinc dopant improves the magnetization saturation of nanoparticles and adsorption efficiency, while optimal content must be maintained. The proposed nanoparticles have the advantage of magnetic filtration in the separation of dye from water, making them a promising material for environmental remediation.

2. Experimental Section

2.1. Chemicals

Iron (III) chloride hexahydrate $FeCl_3 \cdot 6H_2O$ was supplied from Aldrich ACS reagent 97%, and iron (II) chloride tetrahydrate $FeCl_2 \cdot 4H_2O$ p.a. ≥99% (RT) were supplied from Sigma Aldrich (St. Louis, MO, USA). $ZnCl_2 \cdot 4H_2O$ was purchased from Fluka Analytical, pure p.a. >98%. Deionized water with resistivity of 18.2 MΩ·cm at 25 °C was obtained using the Milli-Q ultra-pure water-filtering system from Merck, Germany. Titan yellow and Congo red of analytical grade were purchased from Warchem Sp. z o.o., Poland.

2.2. Synthesis of Nanoparticles

Nanoparticles were synthesized using the wet co-precipitation method, where 1.35 g of $FeCl_3 \cdot 6H_2O$ was placed in a beaker and diluted in 25 mL of Milli-Q water and continuously stirred at 600 rpm at 85 °C. Then, different amounts of the salt of $FeCl_2 \cdot 4H_2O$ and $ZnCl_2 \cdot 4H_2O$ were added depending on the dopant content. The ratio between the salts is presented in Table 1.

Table 1. Mass of particular salts used for synthesis of iron oxide-based nanoparticles.

Source of Ions	$FeCl_3 \cdot 6H_2O$	$FeCl_2 \cdot 4H_2O$	$ZnCl_2 \cdot 4H_2O$
Fe_3O_4	1.35 g	497.0 mg	-
Fe_3O_4@1%Zn		493.6 mg	3.40 mg
Fe_3O_4@2%Zn		490.2 mg	6.80 mg
Fe_3O_4@5%Zn		472.1 mg	24.85 mg
Fe_3O_4@10%Zn		447.3 mg	49.70 mg

2.3. Characterization

The morphology of the nanoparticles was investigated using scanning electron microscopy (SEM), specifically a Zeiss Crossbeam 350 microscope equipped with energy-dispersive X-ray spectroscopy (EDS) and electron-backscattered diffraction (EBSD) detectors. EDS and EBSD data were analyzed using EDAX TEAM software. The powder sample was placed on PELCO® double-sided carbon-based conducing tape, and the tape was glued to an aluminum sample holder. As a second technique, the transmission electron microscopy (TEM) Zeiss Libra 120 Plus (Stuttgart, Germany), operating at 120 kV, was used, where the aqueous suspension was placed on a copper mesh covered with a formvar polymer layer. Then, the sample was left on air (under the fume-hood) for drying. Brunauer–Emmett–Teller (BET) analysis was performed using Asap 2060 micromeritics. The saturation magnetization of SPIONs was measured using a homemade vibrating sample magnetometer (homemade VSM) under the maximum applied field of 11 kOe at room temperature. The semiconductor properties were measured using potentiostat chi660c. X-ray diffraction spectra (XRD) were registered on a Rigaku Ultima IV diffractometer using Cu-Kα (λ = 1.54056 Å) with a step angle of 0.030°, a scanning rate of 0.04285° s^{-1}, and 2θ degree in the range of 10–70°. Adsorption studies were performed using a UV-vis/NIR spectrometer (Perkin Elmer Lambda 1050+). TGA-DTG analysis from room temperature to 500 °C at 5 °C min^{-1} in air was performed on a macro-thermogravimetric system (Montpellier, France) to determine the thermal behaviors of the Fe_3O_4@10%Zn before and after adsorption TY.

2.4. Adsorption Study

The effectiveness of Titan yellow dye removal from aqueous solutions was investigated using UV-vis spectrometry in a wavelength range from 250 nm to 800 nm. Initially, 2 mL of 25 ppm solution (0.36 mM) were exposed to the adsorbent containing different amounts of zinc dopant, and each measurement was performed at least three times. The amount adsorbed onto the nanoparticles was calculated using Equation (1).

$$Amount\ adsorbent = \frac{(c_b - c_a)}{adsorbent\ _{mass}\ (g)} \times V \quad (1)$$

C_a and C_b are concentration before and after adsorption (mg L^{-1}), while V is the volume of the solution (L). Additionally, we also analyzed the effect of the contact time, and the adsorbate concentration.

Maximum adsorption efficiency for all nanostructures was calculated using Equation (2).

$$\%H = \frac{c_0 - c_x}{c_0} \times 100\% \quad (2)$$

where C_0—initial concentration of dye (ppm), C_x—amount of dye adsorbed on the surface of nanoparticles (ppm), and $\%H$—adsorption efficiency (%).

3. Results

3.1. Morphology Studies

As can be seen in Figure 1, the morphology of the particles is similar, where grain-like structures of a size below 20 nm can be distinguished [35]. Nanostructures agglomerate,

while cavities and pores in between the bulk of agglomerates are visible. Since samples are dried in air from aqueous suspension, they tend to agglomerate during the drying process. Despite the differences in the content of dopants, there are minor changes in morphology. EDS mapping revealed the differences in zinc distribution in the sample for particular samples with different doping levels. The morphology is similar to the SEM images described in the literature [36,37].

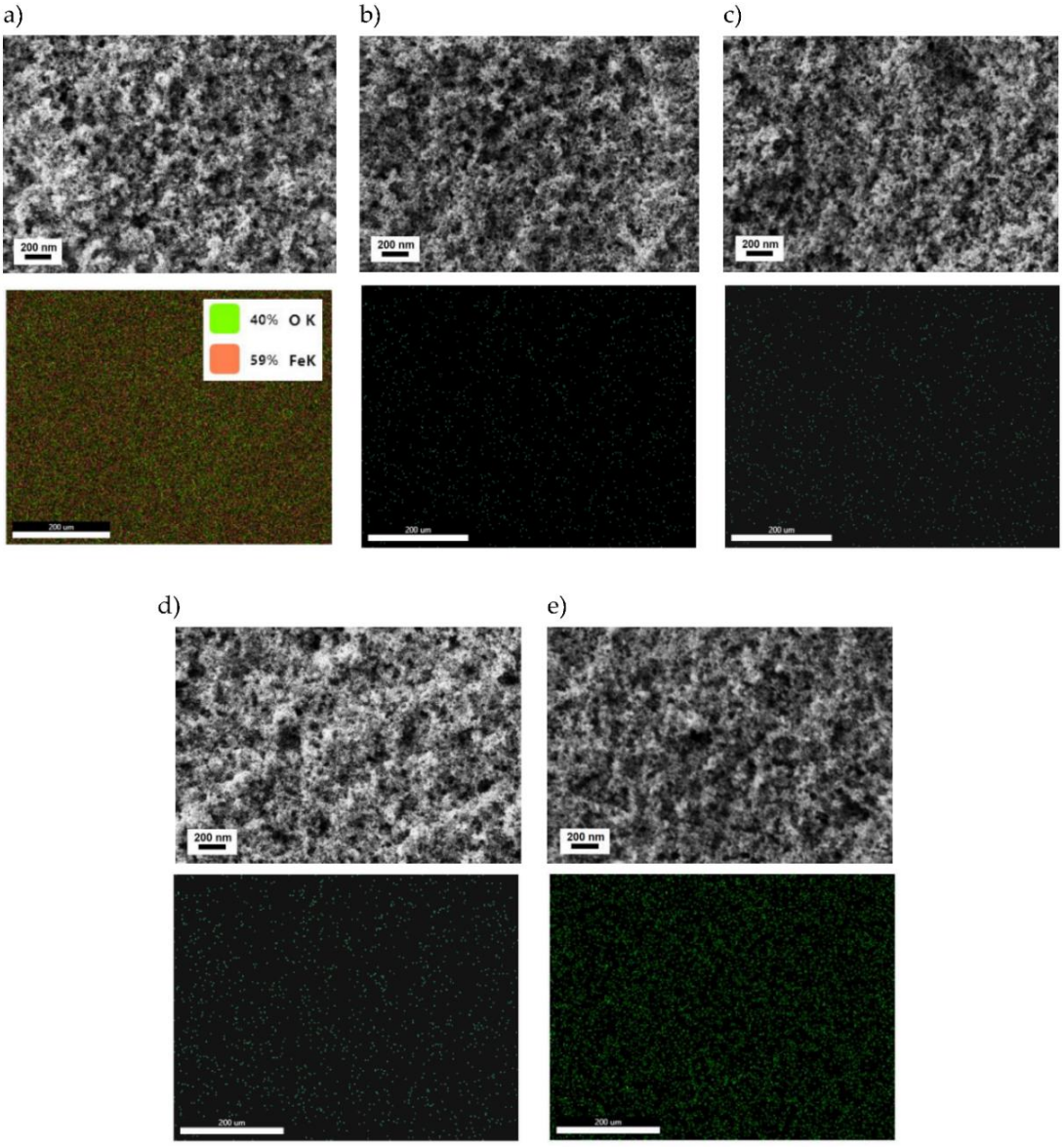

Figure 1. SEM images and EDS map for (**a**) Fe_3O_4, (**b**) Fe_3O_4@1%Zn, (**c**) Fe_3O_4@2%Zn, (**d**) Fe_3O_4@5%Zn, and (**e**) Fe_3O_4@10%Zn. EDS maps for doped samples b–d) show the Zn distribution in the nanoparticles.

Additionally, the features of the particles were examined using TEM. As shown in Figure 2, the size of the average particles is about 15 nm. Nanoparticles form spherical structures, with darker spots the effect of overlapping [38].

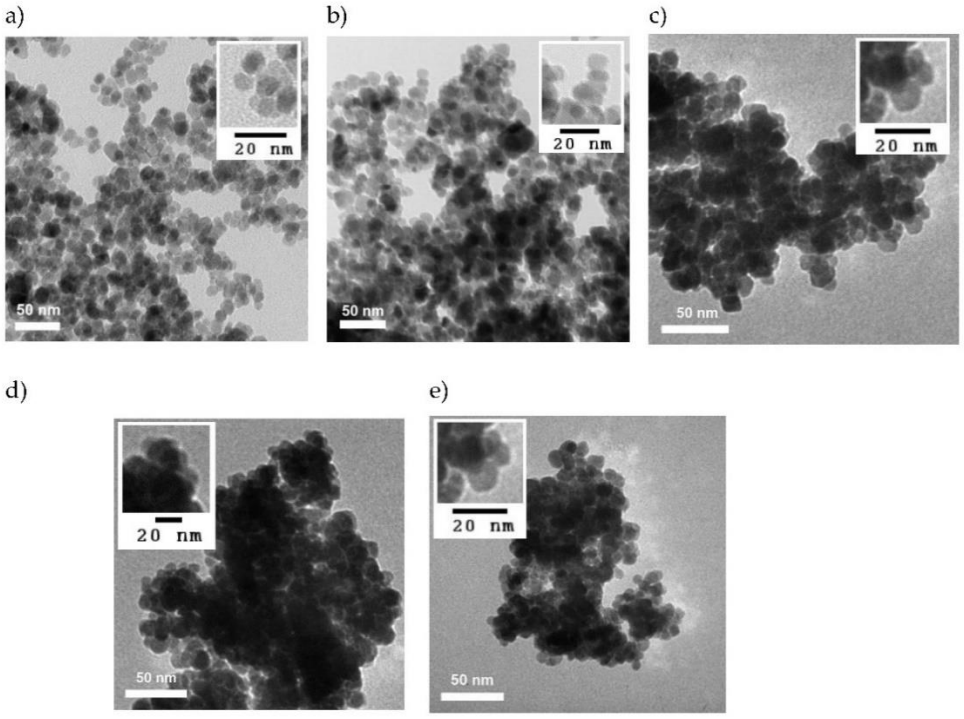

Figure 2. TEM images of (**a**) Fe_3O_4, (**b**) Fe_3O_4@1%Zn, (**c**) Fe_3O_4@2%Zn, (**d**) Fe_3O_4@5%Zn, and (**e**) Fe_3O_4@10%Zn.

3.2. BET Analysis

The BET-specific surface area and micropore area of the nanoparticles were investigated using BET (Brunauer–Emmett–Teller) isotherms. Based on the adsorption–desorption isotherms, the porosity of the five samples was analyzed from the N_2 adsorption method using an ASAP 2060 micromeritics analyzer. The specific surface area was determined using the BET method, and the microporous area and volume were estimated using a t-plot. The mesoporous area and volume, estimated using BJH, was also conducted. Results are given in Table 2. It can be seen that all five samples had quite similar values of S_{Total}, ranging from 85.7 to 101.5 $m^2\ g^{-1}$, where the highest values were obtained for pristine Fe_3O_4 and Fe_3O_4@10%Zn. Moreover, their S_{Micro} and V_{Micro} values were close to zero, suggesting that the porosity of these samples is not given by the micropores, but mostly by the mesopores formed by the aggregates inside the samples. The materials with different percentage of Zn (from 1% to 10%) had mostly the same mesoporous structures, expressed by the similarities in S_{Meso}, V_{Meso} and d_{Mean} pores, as seen in the literature [39,40]. However, the results of Fe_3O_4 indicated that the pristine material had a higher mesopore volume, which was composed of larger amounts of mesopores compared to the materials doped with Zn. It is suggested that the Zn content added to the Fe_3O_4 was attached to the macropores reducing the pore size and volume of these structures. However, the highest surface area was recorded for Fe_3O_4 and Fe_3O_4@10%Zn, which agrees with the TY adsorption studies (these samples removed dye at the highest efficiency).

Table 2. Surface areas and pore volumes of five samples.

Sample	S_{Total} ($m^2\ g^{-1}$)	S_{Micro} ($cm^2\ g^{-1}$)	S_{Meso} ($cm^2\ g^{-1}$)	V_{Meso} ($cm^3\ g^{-1}$)	$d_{Mean\ pore}$ (nm)
Fe_3O_4	97.9	0	100.4	0.17	6.78
Fe_3O_4@1%Zn	85.7	2.3	54.5	0.03	2.41
Fe_3O_4@2%Zn	93.1	0	70.0	0.04	2.29
Fe_3O_4@5%Zn	91.4	1.6	66.9	0.04	2.30
Fe_3O_4@10%Zn	101.5	5.2	63.3	0.04	2.40

3.3. Crystallinity

Due to the different compositions of synthesized particles, the crystal structure was determined using the X-ray diffraction (XRD) technique. As shown in Figure 3, the XRD diffractograms of the samples doped with zinc are similar, while for undoped Fe_3O_4, minor shifts in the position of particular patterns are visible. All the samples exhibited the typical crystal structure of Fe_3O_4 (JCPDS card 02-088-0315), including peaks at 30.1°, 35.4°, 43.1°, 53.5°, 57.1°, and 63.2°. These can be ascribed to the (220), (311), (400), (422), (511), and (440) planes, respectively [38,41–43]. At the same time, in all doped samples, the peak at 30.1° is increased, corresponding to the (220) plane of the $Zn_xFe_{(1-x)}Fe_2O_4$ [23,44]. Aghazadeh also presented the growth of peaks after the Zn doping of iron oxide [45]. Similar results were presented by Paz-Díaz et al. [46] and Shanmugavaniand and Selvan [47]. As there are no additional peaks in the diffractograms for a multiphase system as in the literature [48–50], it can be assumed that the particles contain one phase. The particles obtained within this work were estimated using the Debye–Scherrer Equation (3).

$$D=(K\lambda/\beta \cos \theta), \quad (3)$$

where D is the size of the crystallite (nm), K is known as the Scherer's constant (K = 0.94), λ is the X-ray wavelength (λ = 1.54056 Å), β is full width at half maximum (FWHM) of the diffraction peak, and θ is the angle of diffraction.

The following size of crystallites were determined: Fe_3O_4—11.01 nm, Fe_3O_4@1%Zn—12.74 nm, Fe_3O_4@2%Zn—12.77 nm, Fe_3O_4@5%Zn, 11.98 nm, and Fe_3O_4@10%Zn—10.48 nm.

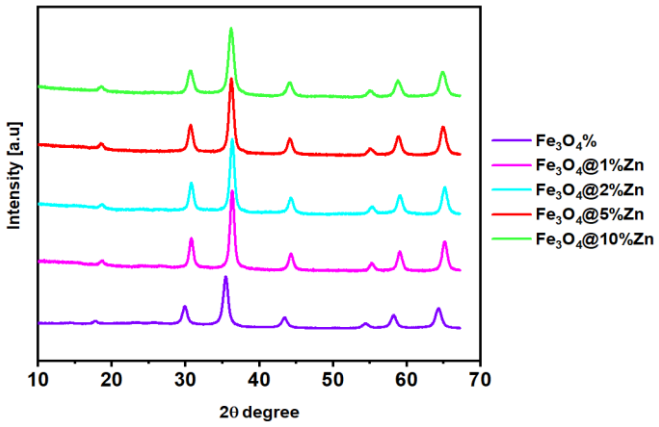

Figure 3. XRD patterns of Fe_3O_4, Fe_3O_4@1%Zn, Fe_3O_4@2%Zn, Fe_3O_4@5%Zn, and Fe_3O_4@10%Zn.

3.4. Magnetic Properties

The magnetic properties of the nanoparticles were evaluated using a homemade vibrating sample magnetometer, where the measurements were recorded at 300 K. The hysteresis loops of the magnetic samples are shown in Figure 4. The magnetization increases with the increase of zinc content in the crystal structure. The saturation magnetization (M_s) values are in the order 60.89 emu g^{-1} for Fe_3O_4, 63.32 emu g^{-1} for Fe_3O_4@1%Zn, 64.28 emu g^{-1} for Fe_3O_4@2%Zn, 68.69 emu g^{-1} for Fe_3O_4@5%Zn, and 68.72 emu g^{-1} for Fe_3O_4@10%Zn. Similar values of saturation magnetization (M_s) and low coercivity (H_c) of all samples were recorded, and be ascribed to superparamagnetic properties. The obtained values are similar to the data described in the literature [50,51]. It reveals the highest effect of zinc dopant with 10% wt.%. on the saturation magnetization.

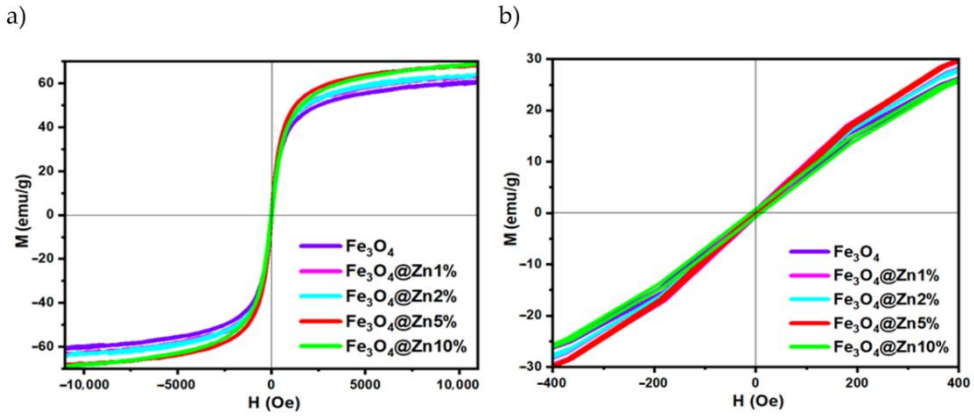

Figure 4. Magnetization curves of Fe_3O_4, Fe_3O_4@1%Zn, Fe_3O_4@2%Zn, Fe_3O_4@5%Zn, and Fe_3O_4@10%Zn at (**a**) full H range (from −10 kOe to 10 kOe), and (**b**) narrow H range (from −400 Oe to 400 Oe).

3.5. Optical Absorption Properties

The band gap of the prepared nanoparticles was determined using a UV-vis spectrometer. The optical absorption spectra relating to the transition of the electrons from the valence band to the conduction band were recorded to estimate the band-gap energy E_g for SPIONs. Based on the UV-vis spectra and Tauc equation (see Equation (4)) the optical band-gap energy was calculated.

$$\alpha h\nu = K(h\nu - E_g)_n \quad (4)$$

where: α is the absorption coefficient of semiconductor, $h\nu$ is a photon energy, K is the frequency-independent material constant, and exponent n is the electronic transition, where it depends on the nature of transition in the semiconductor that is equal to ½ allowing for direct transition.

The band gap for undoped Fe_3O_4 is equal to 2.35 eV, and similar values were also recorded for the 1–5% dopants. However, for SPION@10%Zn, the band gap had a lower value. The corresponding Tauc plots yielding the energy band gap are in good agreement with the literature [52]. However, as the optical properties depend on experimental conditions, the values can be easily disturbed. Figure 5 illustrates the Tauc plot for the SPIONs with different dopant content, and it is clearly seen that the band-gap energy (an average value from three measurements) for all samples is almost the same. The values for samples are also presented in Table 3.

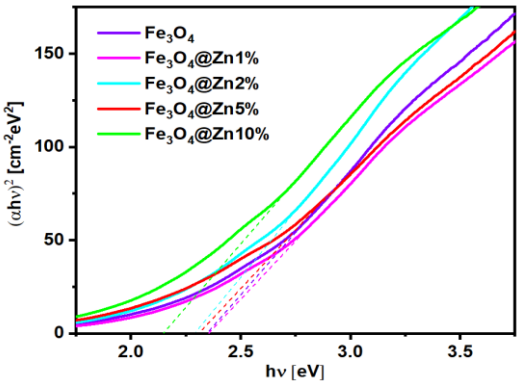

Figure 5. Tauc plot for the SPIONs with different content of zinc dopant.

Table 3. Band-gap value for samples with different concentration of zinc in the crystal structure of nanoparticles measured three times for each sample type.

Nanoparticles	Band-Gap Energy [eV]
Fe_3O_4	2.35 ± 0.08
Fe_3O_4@1%Zn	2.35 ± 0.10
Fe_3O_4@2%Zn	2.34 ± 0.29
Fe_3O_4@5%Zn	2.33 ± 0.30
Fe_3O_4@10%Zn	2.24 ± 0.08

3.6. Adsorption Studies of Titan Yellow

Titan yellow dye has two characteristic absorption peaks: the first is located at 405 nm, and the second is at about 333 nm. The effect of the Fe_3O_4 doped with Zn nanoparticles on the removal of Titan yellow was evaluated by adding various amounts of adsorbent—10, 20, 40, 100, and 200 mg—into beakers containing 20 mL with an initial dye concentration of 25 mg L^{-1} at pH 7.0. The dye was exposed to the adsorbent (adsorbent was added to the beaker and the solution was not mixed) for 30 min. Prior to UV-vis measurement, the nanoadsorbents were placed in a beaker filled with dye solution. Then, the suspension was mixed mechanically and, after a particular contact time, the nanoadsorbent was separated magnetically, and collected at the bottom of the beaker. Next, after nanoadsorbent treatment, the solution was removed from the beaker using a pipette and placed in a quartz cuvette.

Measurements were performed for all SPIONs containing 0%, 1%, 2%, 5%, and 10% zinc dopant. By increasing the amount of the adsorbent, the absorbance of dye remaining in the solution decreased as more active sites on the SPIONs' surface became available for absorbing the molecules of dye, as shown in Figure 6. The presented spectra were recorded for 30 min contact time as an overview to present the absorbance drop with an increase of the adsorbent mass for a particular type of sample. The survey spectra for doses affected TY adsorption. Based on the recorded spectra, 20 mg was proposed to be used in Titan yellow adsorption studies.

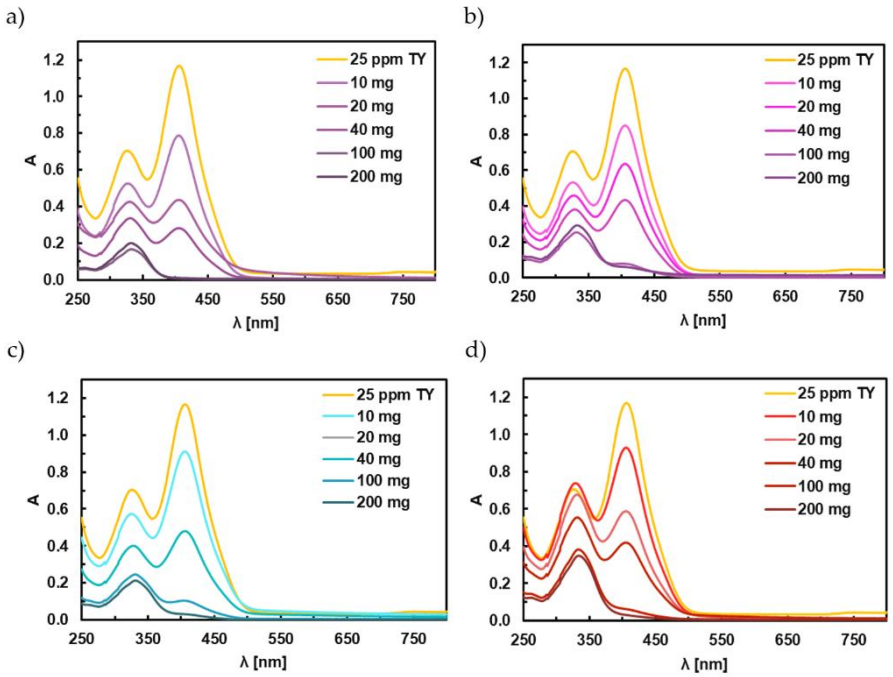

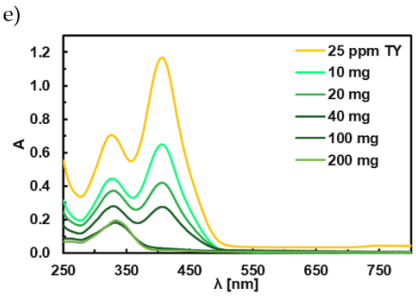

Figure 6. Survey UV-vis spectra adsorption of Titan yellow dye by (**a**) Fe_3O_4, (**b**) Fe_3O_4@1%Zn, (**c**) Fe_3O_4@2%Zn, (**d**) Fe_3O_4@5%Zn, and (**e**) Fe_3O_4@10%Zn nanoparticles in different mass ratios after 30 min in pH 7.

Within this part of adsorption studies, the optimal dose of particles was investigated. Based on the recorded spectra, a more intensive peak was used to optimize the experimental conditions for optimal dye removal from solutions. Figure 7 reveals the effect of mass and dopant on the effectiveness of dye adsorption, where each measurement was repeated a minimum of three times, and the average values are presented on the graphs. The curves present maximum adsorption efficiency, %H, in the function of time, where each dopant was marked with different colors. As can be seen in Figure 7a, the effectiveness of the TY from the highest, in order, is Fe_3O_4@10%Zn > Fe_3O_4 > Fe_3O_4@1%Zn > Fe_3O_4@2%Zn > Fe_3O_4@5%Zn for the 10 mg, 20 mg, and 40 mg of the adsorbent dose. With the following increase of the adsorbent dose, still, Fe_3O_4 and Fe_3O_4@10%Zn absorb the dye similarly with the highest efficiency.

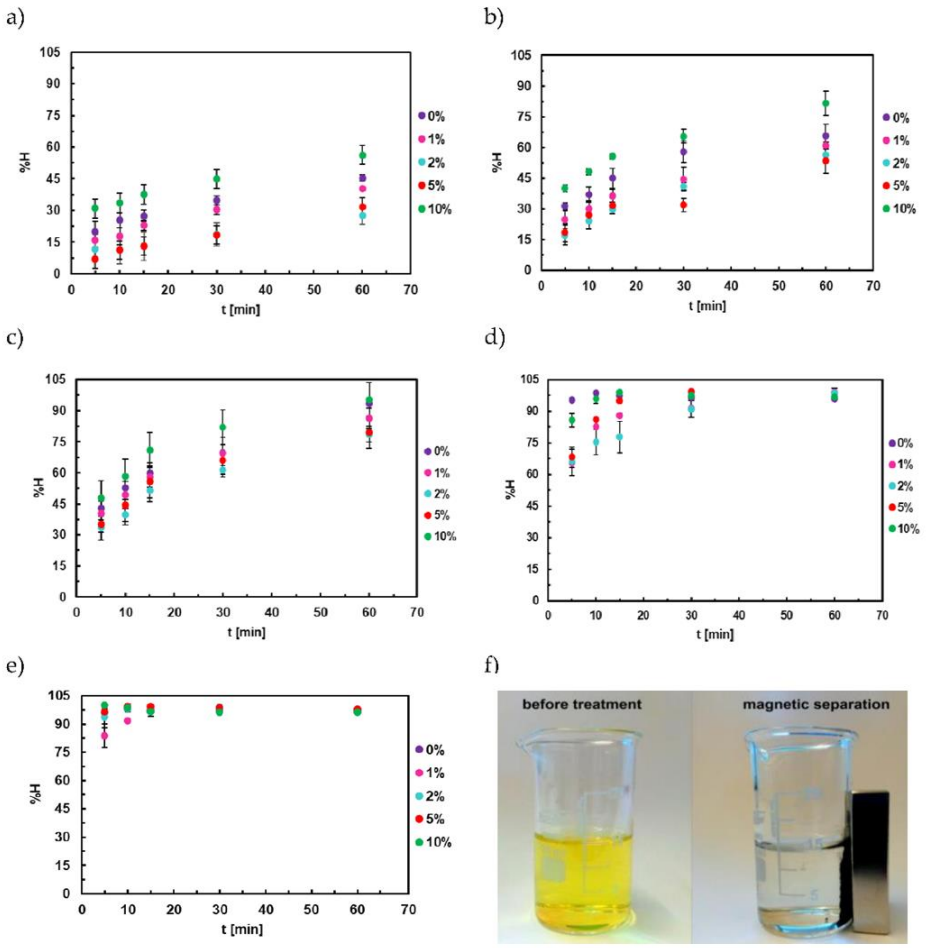

Figure 7. UV-vis adsorption efficiency of Titan yellow dye after (**a**) 10 mg, (**b**) 20 mg, (**c**) 40 mg, (**d**) 100 mg, (**e**) 200 mg nanoparticles addition in function of time, and (**f**) TY solution after treatment and magnetic separation with Fe_3O_4@10%Zn.

After the mass-effect studies, UV-vis measurements were followed with the contact time of the nanostructures on the adsorbate, where %H was measured as a function of time. Based on the mass-effect studies, it can be seen that 100 and 200 mg doses are large enough to remove the pollutant. However, from an economical point of view, such an amount is not cost-effective, so the 20 mg dose was proposed. Moreover, for these data, the kinetics of the process was examined because, at higher masses, the kinetic adsorption process is too fast, and it would be hard to notice the kinetic profile. The measurements were performed at the same adsorbate concentration. Figure 8 shows the highest effect for pristine iron oxide and SPIONs doped with 10% zinc, where within 60 min the maximal adsorption efficiency was observed.

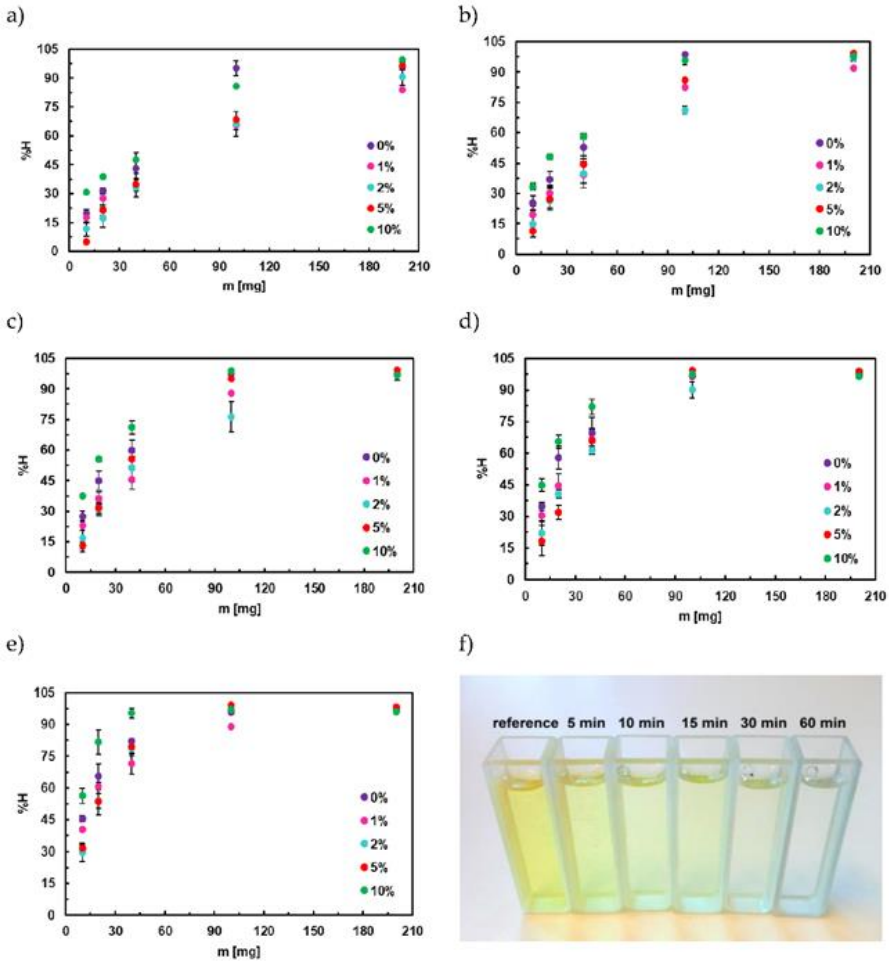

Figure 8. UV-vis adsorption efficiency of Titan yellow dye with contact time (**a**) 5 min, (**b**) 10 min (**c**) 15 min, (**d**) 30 min, and (**e**) 60 min in function of different mass ratios, (**f**) different contact time for Fe_3O_4@10%Zn.

3.7. Adsorption Kinetics of Titan Yellow

Based on the experimental results obtained within the UV-vis spectrometry, the kinetics of the adsorption mechanism was investigated; see Figure 9. The kinetics of the adsorption processes were determined using Lagergren's pseudo-first-order law and McKay–Ho's pseudo-second-order law mode given in Equations (5) and (6), respectively:

$$ln(q_e - q_t) = \ln(q_e) - k_1 t \quad (5)$$

where q_t (mg g^{-1}) is the adsorption capacity at time t, q_e (mg g^{-1}) is the adsorption capacity at equilibrium, and k_1 (min^{-1}) is the pseudo-first-order adsorption rate constant.

$$\frac{t}{q_t} = \frac{1}{k_2 q_e^2} + \frac{t}{q_e} \quad (6)$$

where k_2 (g min^{-1} mg^{-1}) is the pseudo-second-order rate constant for adsorption.

As shown in Figure 9, based on the R^2 values for pure iron oxide, the adsorption process follows the kinetics of the pseudo-second order. The adsorption kinetics for undoped iron oxide is consistent with the literature [35,53]. The value R^2 for 10% of zinc is similar to the pseudo-first order; however, the pseudo-second-order sorption can be approximated more appropriately by the pseudo-second-order kinetic model; see Figure 10. The samples containing dopants lower than 10% undergo the pseudo-first-order kinetics.

Pseudo-first order of adsorption process:

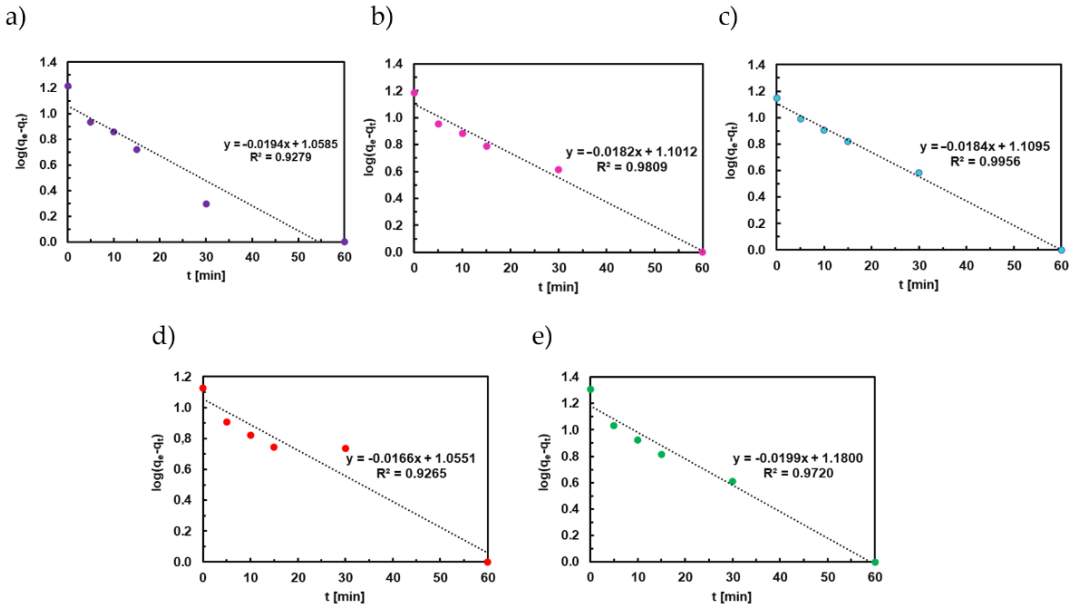

Figure 9. Adsorption data modeled using kinetic Lagergren's pseudo-first-order law for (**a**) Fe_3O_4, **(b)** Fe_3O_4@1%Zn, (**c**) Fe_3O_4@2%Zn, (**d**) Fe_3O_4@5%Zn, and (**e**) Fe_3O_4@10%Zn nanoparticles.

Pseudo-second order of adsorption kinetics:

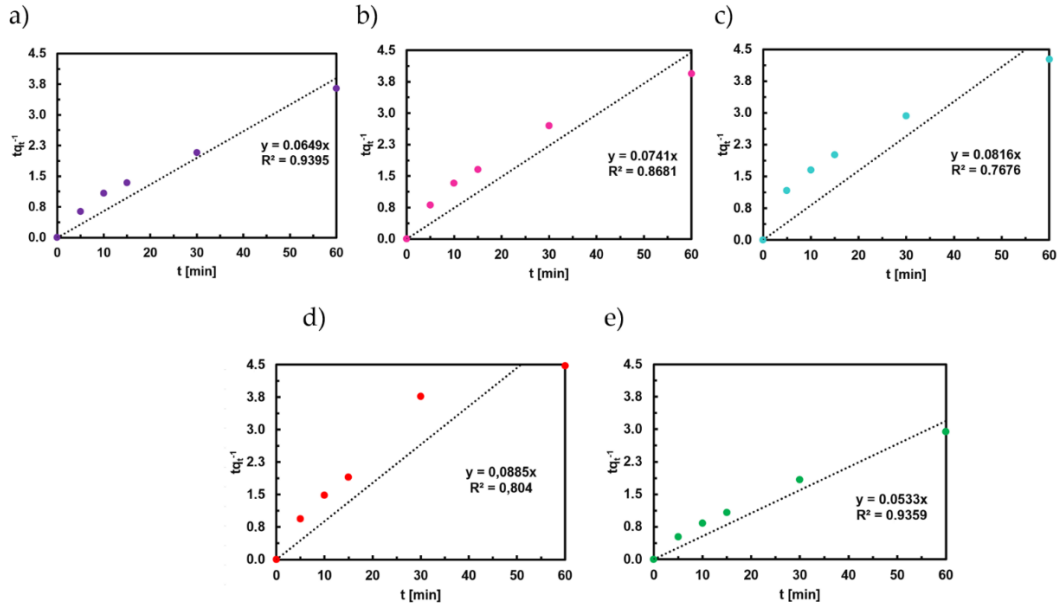

Figure 10. Adsorption data modeled using kinetic McKay and Ho's pseudo-second-order law for (**a**) Fe_3O_4, (**b**) Fe_3O_4@1%Zn, (**c**) Fe_3O_4@2%Zn, (**d**) Fe_3O_4@5%Zn, and (**e**) Fe_3O_4@10%Zn nanoparticles.

Additionally, thermogravimetric analysis (TGA) was performed for the samples removing TY most efficiently, i.e., Fe_3O_4 and Fe_3O_4@10%Zn. Measurements were taken on samples before adsorption and after dye removal in the optimized conditions from the 25 ppm of TY. As can be seen in Figure 11, in all samples, mass loss is observed. The initial mass loss above 100 °C corresponds to the desorption of water, while for the samples after dye treatment the weight loss associated with the thermal degradation of Titan yellow. Complementary to the UV-vis studies, TGA analyses confirms the adsorption of TY on the nanoparticles. As the TY degrades under the thermal treatment, nanoparticles can be reused for adsorption studies.

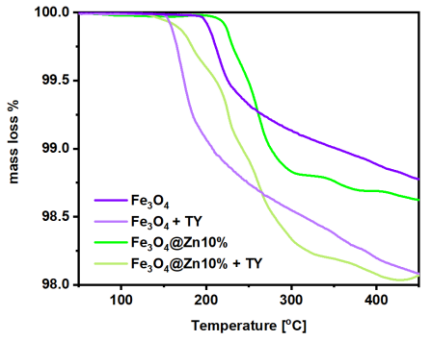

Figure 11. Thermogram for the Fe_3O_4 and Fe_3O_4@10%Zn before the TY adsorption, and after the dye adsorption onto SPION surfaces.

3.8. Adsorption Isotherm of Titan Yellow

The experimental data obtained from the adsorption of Titan yellow (TY) using Fe_3O_4 and Fe_3O_4@10%Zn were fitted into the non-linear equation of Langmuir, Freundlich, and Redlich-Peterson adsorption isotherms. Therefore, the plot of the amount adsorbed at equilibrium (q_e) versus the equilibrium adsorbate concentrations (C_e) is shown in Figure 12. The non-linear equations of Langmuir, Freundlich, and Redlich-Peterson are presented in Equations (7)–(9), respectively.

$$q_e = \frac{q_{max} C_e K_L}{(1+K_L C_e)} \quad (7)$$

$$q_e = K_F C_e^{1/n_F} \quad (8)$$

$$q_e = \frac{K_{RP} C_e}{(1 + a_{RP} C_e^{g})} \quad (9)$$

where C_e is the equilibrium concentration (mg L^{-1}), q_e is the equilibrium adsorbed (mg g^{-1}), q_{max} is the maximum adsorption capacity (mg g^{-1}), K_L is Langmuir equilibrium constant (L mg^{-1}), K_F is the Freundlich constant (mg g^{-1} (mg L^{-1})$^{-1/nF}$), n_F is the dimensionless exponent of Freundlich, where K_{RP} (L g^{-1}) and a_{RP} (mg L^{-1})$^{-g}$ are the Redlich-Peterson constants and g is dimensionless.

Langmuir and Freundlich assume homogeneous and heterogeneous adsorption processes, while Redlich-Peterson made up the limitations of both Langmuir and Freundlich isotherms by incorporating the features of the two isotherms [54]. The parameters of the equations, adjusted coefficient of determination ($R^2_{adjusted}$), and standard deviation (SD) obtained from the curve fit of the isotherms are shown in Table 4. The respective values of the $R^2_{adjusted}$ and SD of Langmuir and Redlich-Peterson for Fe_3O_4@10%Zn are approximately near each other; this implies that the two isotherms can accurately describe the adsorption of TY on Fe_3O_4@10%Zn. In the case of Fe_3O_4, $R^2_{adjusted}$ of Redlich-Peterson is higher than that of Langmuir, while the SD is lower. However, to ascertain the conformation of the experimental data with Redlich-Peterson, the value of g must be less than 1 [55]. As shown in Table 1, the value of g obtained for Fe_3O_4@10%Zn is less than 1, which indicates that the Redlich-Peterson (RP) isotherm model is suitable for explaining the adsorption process of TY on the Fe_3O_4@10%Zn. When g in RP equations is equal to 1, then it reduces to Langmuir. Therefore, the overlapping of Langmuir and RP in Figure 12b could be because g (0.9817) of RP is close to 1. Despite the higher value of $R^2_{adjusted}$ and lower SD of Redlich-Peterson compared to Langmuir for Fe_3O_4, the value of g that is higher than 1 makes it inapplicable for the adsorption process of TY on Fe_3O_4. The experimental data are also not well fitted into the Freundlich isotherm for both Fe_3O_4 and Fe_3O_4@10%Zn.

The monolayer adsorption capacity Fe_3O_4@10%Zn for the removal of TY is 43 mg g^{-1}, while that of Fe_3O_4 is 30 mg g^{-1}, which are higher than some of the adsorbents reported in the literature (Table 5). The higher adsorption capacity of Fe_3O_4@10%Zn than pristine Fe_3O_4 is related to the difference in their specific surface area.

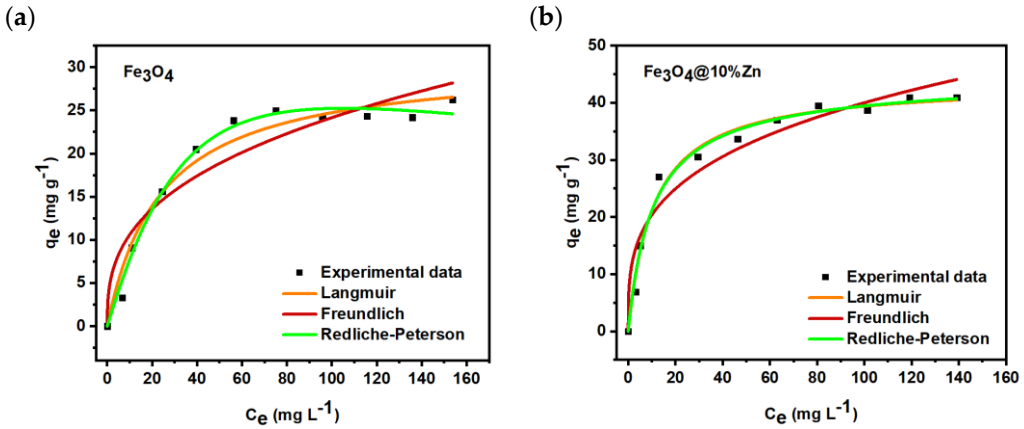

Figure 12. Isotherm modeling and experimental data for (**a**) Fe_3O_4 and (**b**) Fe_3O_4@10%Zn nanoparticles.

Table 4. Adsorption parameters.

Parameters	Fe_3O_4	Fe_3O_4@10%Zn
Langmuir		
q_{max} (mg g^{-1})	30.0	43.0
K_L (L mg^{-1})	0.041	0.094
$R^2_{adjusted}$	0.966	0.985

SD (mg g^{-1})	1.72	1.77
Redlich-Peterson		
K_{RP} (L g^{-1})	0.843	4.28
a_{RP} (mg L^{-1})$^{-g}$	0.004	0.107
g	1.39	0.981
$\mathbf{R^2_{adjusted}}$	0.985	0.983
SD (mg g^{-1})	1.13	1.86
Freundlich		
$\mathbf{K_F}$ (mg g^{-1}) (mg L^{-1})$^{-1/nF}$	4.66	10.36
$\mathbf{n_F}$	2.79	3.40
$\mathbf{R^2_{adjusted}}$	0.889	0.937
SD (mg g^{-1})	3.14	3.61

Table 5. Comparison of the maximum adsorption (q_{max}) of different adsorbents for the removal of Titan yellow.

Adsorbents	q_{max} (mg g^{-1})	References
$NiFe_2O_4$	19.193	[56]
Chitosan	58.76	[57]
Saccharum spontaneum	3.984	[58]
Walnut Husks	7.6982	[59]
Bio-Waste Aloe vera Leaves	55.25	[60]
Fe_3O_4	30.0	This work
Fe_3O_4@10%Zn	43.0	This work

3.9. Effect of pH and Ionic Strength on the Adsorption of TY

The role that effect of pH plays in understanding the adsorption process of any contaminant, especially for the wastewater treatment [61]. Given this, the study of the effect of pH on the adsorption of TY by Fe_3O_4@0% Zn and Fe_3O_4@10% Zn was investigated. The two materials were chosen based on their better performance compared to other synthesized materials used in this research work. The results are shown in Figure 13a**.** Increasing the solution pH decreases the amount of TY that was absorbed by Fe_3O_4@0% Zn and Fe_3O_4@10% Zn. The highest amounts, 23 and 24.4 mg g^{-1} of TY, were absorbed by Fe_3O_4@0% Zn and Fe_3O_4@0% Zn, respectively, at pH 2. At pH 10, the amount reduced to 5.7 and 7.9 mg g^{-1} by Fe_3O_4@0% Zn and Fe_3O_4@10% Zn, respectively. The reason for this is the anionic nature of TY dye [62], which is expected to be favorably adsorbed on a positively charged surface of an adsorbent. Our previous study [35] showed that iron oxide nanoparticles are positively charged at pH below 7. Therefore, the highest amount adsorbed at pH below 7 is due to an electrostatic interaction between the anionic TY dye and the positively charged Fe_3O_4@0% Zn and Fe_3O_4@10% Zn. One would expect an electrostatic repulsion at pH 8 and 10, but TY was adsorbed at these pH values, by Fe_3O_4@0% Zn and Fe_3O_4@10% Zn, though lower than the amount adsorbed at acidic pH values. The explanation for this is provided in the further discussion on the effect of ionic strength.

In textile industries, salts such as NaCl are used during the dyeing process, which causes effluents from this industry to contain salts [63]. The effects of salts in terms of ionic strength on the adsorption of TY has been studied by varying the concentration of NaCl within the range of 0.04 to 0.2 mol L^{-1}. Since the trend of adsorption of TY by Fe_3O_4@0% Zn and Fe_3O_4@10% Zn with respect to pH followed the same pattern, we investigated the effect of ionic strength on Fe_3O_4@10% Zn as a model for other materials, since it performed better that the rest of the materials. As shown in Figure 13b**,** the amount of TY adsorbed by Fe_3O_4@10% Zn increased from 20.9 to 24.1 mg g^{-1} in the presence of 0.04 mol L^{-1} of NaCl. Further increase in ionic strength did not lead to a significant increase in the adsorption of

TY. This shows that the presence of salts in dye effluent that contains TY will promote favorable adsorption. It is worth noting that the presence of ionic strength could increase, decrease or not affect the adsorption of organic molecules [64,65]. Whenever the presence of salts leads to an increase in the adsorption of organic molecules, as with TY, hydrophobic interaction has been credited with the adsorption process [65,66]. Based on the results from the effect of pH and ionic strength, this implies that both electrostatic attraction and hydrophobic interaction are the two mechanisms that are involved in the adsorption of TY. Therefore, the adsorption of TY at alkaline pH is due to the involvement of these two adsorption mechanisms.

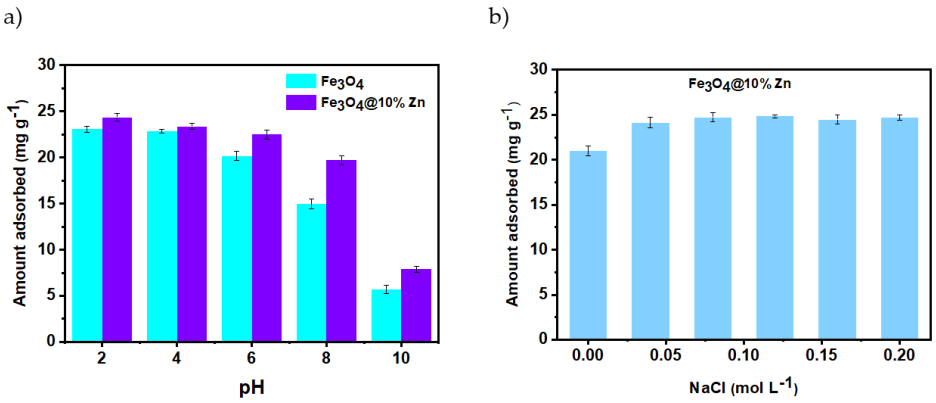

Figure 13. The effect of pH (**a**) and the ionic strength (**b**) on the adsorption of Titan yellow.

4. Photocatalytic Studies

Since the nanoparticles used in this work are semiconducting, they can be used not only for TY removal via adsorption but also for photocatalytic degradation. Based on adsorption studies, the optimal experimental conditions were proposed. So far, the photocatalytic effect of nanostructures on dye degradation of the 20 mg of nanoparticles of all dopants was based on the 20 mL of the 25-ppm Titan yellow solution. Then, the solution was exposed to a mercury lamp (UV-vis source) for 60 min with the fan cooling set up to protect the solution from overheating. The photodegradation of the TY was investigated as complementary to the adsorption studies, where dark adsorption was performed prior to photodegradation to present only the photodegradation effect.

In contrast to the literature where, for example, Vidya et al. proposed the use of zinc oxide nanoparticles to degrade 20-ppm Titan yellow solution with 60 mg adsorbent, in this work, only 20 mg were used to reach similar effectiveness [62,67]. As the highest effectiveness of the adsorption was proved for undoped Fe_3O_4 and Fe_3O_4@10%Zn nanoparticles, the same conditions were proposed to investigate the effectiveness of the TY degradation. Figure 14a shows the photocatalytic efficiency for all samples from 0% to 10% zinc dopants, where it is clearly seen that the highest effectiveness of the particles in the TY treatment is observed for Fe_3O_4@10%Zn and Fe_3O_4, respectively. Undoped iron oxide and 1–2% doped nanoparticles have similar results. The Fe_3O_4@10%Zn reduces the amount of dye in the water solution from 25 ppm to 6.6 ppm, reaching 74% removal efficiency, while Fe_3O_4@5%Zn reaches about 62% efficiency. At this point, analogically to the %H determination without the additional exposition of the solution on the UV irradiation, measurements were also performed under a UV-vis lamp. The reference sample, containing only TY solution, was also illuminated at the same time, without SPION addition to check the degradation of the dye, and no changes in the spectra were recorded. Figure 14b shows the efficiency of the photodegradation process after 60 min of exposition on the samples under a UV-vis light compared with the results obtained for adsorption studies without external light exposition. Interestingly, the highest efficiency is recorded only for Fe_3O_4@5%Zn; however, the effect is only slightly higher than without light exposure. The low effectiveness of the samples on

the photocatalytic effect are caused by a too-low band-gap energy compared to the location of the particular TY bands corresponding to the absorption of a certain wavelength of light. Therefore, the proposed samples work better as adsorbents than as photocatalysts for TY treatment, so for photocatalytic studies, material with broader band-gap energy or compounds absorbing blue–green light should be used.

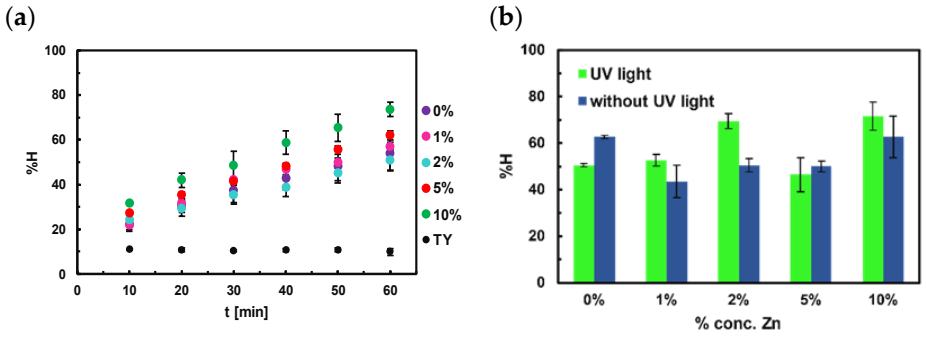

Figure 14. Efficiency of (**a**) photodegradation process by Fe_3O_4, Fe_3O_4@1%Zn, Fe_3O_4@2%Zn, Fe_3O_4@5%Zn, and Fe_3O_4@10%Zn nanoparticles after 60 min exposure time and (**b**) photo-assisted removal of TY process in pH equal 7.

4.1. Adsorption Studies of Congo Red

As the removal of Titan yellow, which is a sulphonic dye, was effective, the following studies were also performed for Congo red—another sulphonic dye—which can also be commonly found in wastewater [68]. Figure 15a presents the absorption spectra for the 20-ppm Congo red solution treated within 20 mg of adsorbent for contact time from 5 to 120 min. Based on spectra similar to TY, efficiency H% was estimated. The highest efficiency was observed for the sample doped with 10% of zinc, reaching about 80% of H%, see Figure 15b. As follows, Figure 15c shows the Congo red solution before treatment and post-treatment with adsorbent.

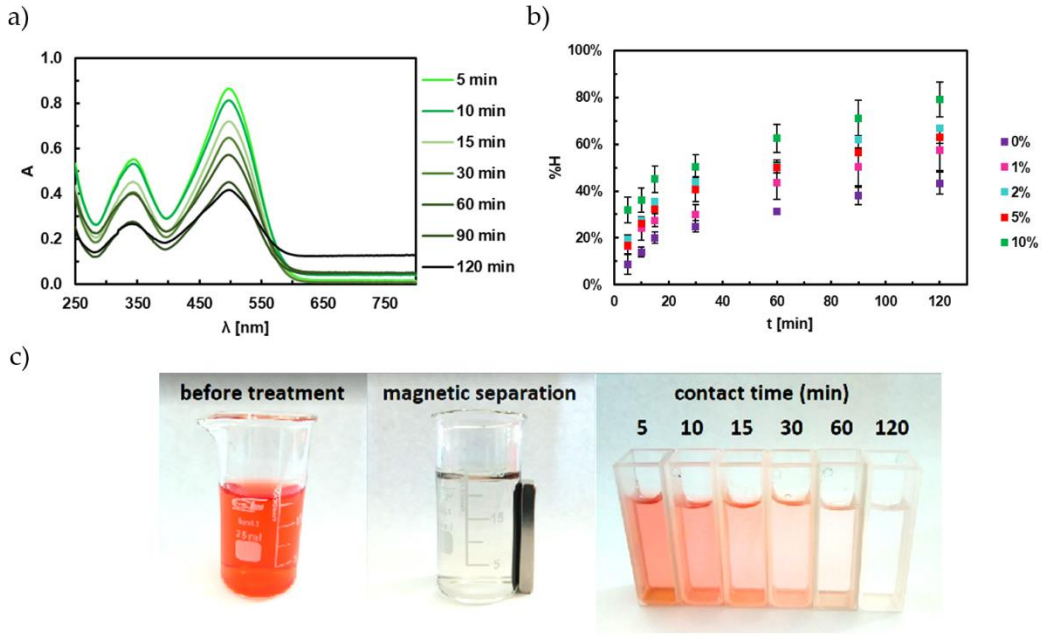

Figure 15. (**a**) UV-vis spectra adsorption of Congo red dye by Fe_3O_4@10%Zn nanoparticles with 20 mg adsorbent dose in function of contact time, (**b**) removal efficiency for 20 mg nanoparticles dose at 120 min, and (**c**) solution before and after treatment in pH 6.

4.2. Adsorption Kinetics of Congo Red

Next, the kinetics of CR adsorption was investigated. As can be seen in Figure 16a-b, the Fe_3O_4 and Fe_3O_4@1%Zn nanoparticles undergo first-order kinetics during adsorption of CR. The following graphs presented in Figure 16c–e corresponding to the Fe_3O_4@2%Zn, Fe_3O_4@5%Zn, and Fe_3O_4@10%Zn, respectively, where the results were compared with the pseudo-second-order kinetics presented in Figure 17, based on the R^2 fitting.

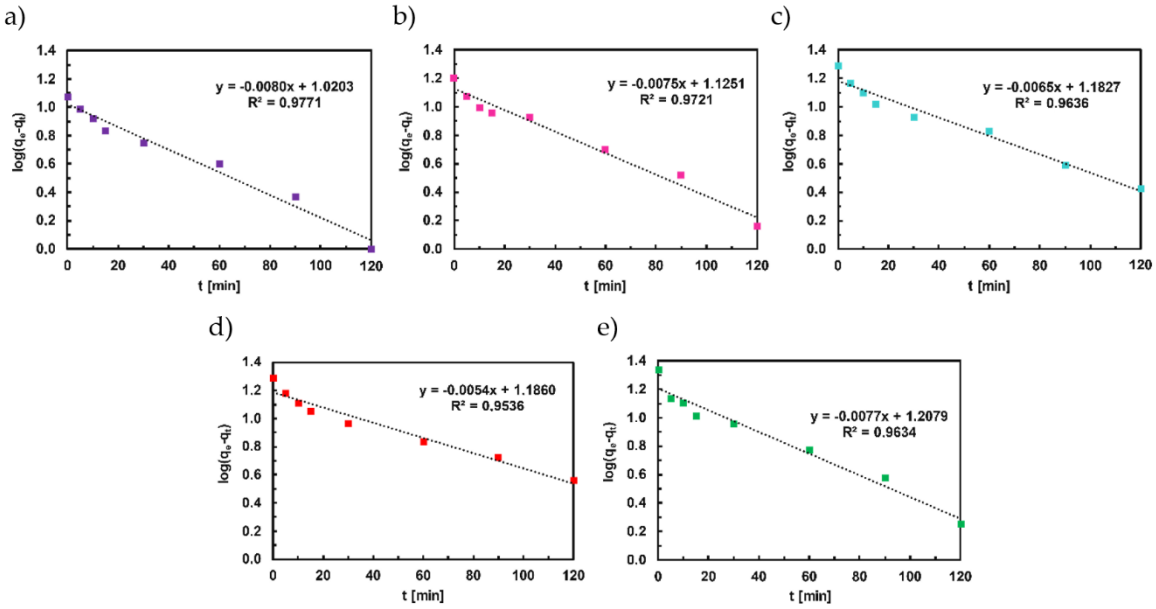

Figure 16. Adsorption data modeled using kinetic Lagergren's pseudo-first-order law for (**a**) Fe_3O_4, (**b**) Fe_3O_4@1%Zn, (**c**) Fe_3O_4@2%Zn, (**d**) Fe_3O_4@5%Zn, and (**e**) Fe_3O_4@10%Zn nanoparticles in pH equal 6.

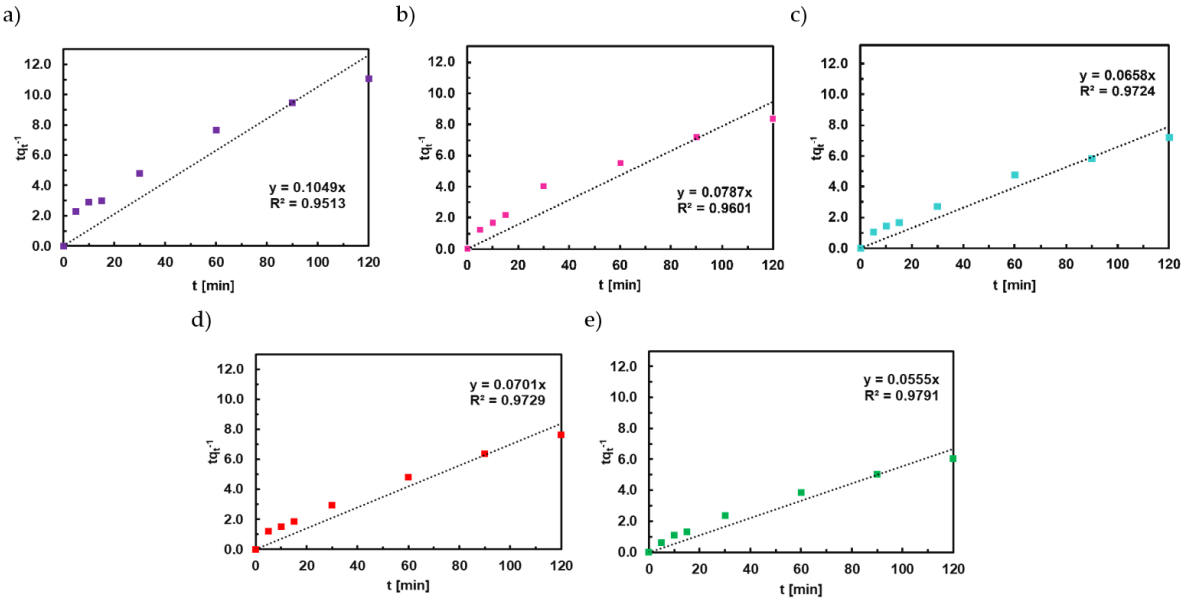

Figure 17. Adsorption data modeled using kinetic McKay and Ho's pseudo-second-order law for (**a**) Fe_3O_4, (**b**) Fe_3O_4@1%Zn, (**c**) Fe_3O_4@2%Zn, (**d**) Fe_3O_4@5%Zn, and (**e**) Fe_3O_4@10%Zn nanoparticles in pH equal 6.

Adsorption kinetics models for Fe_3O_4@2%Zn, Fe_3O_4@5%Zn, and Fe_3O_4@10%Zn undergo pseudo-second adsorption, which agrees with the literature [69].

4.3. Effect of pH and Ionic Strength on the Adsorption of CR

The adsorption study of Congo red dye on the proposed adsorbent requires a separate approach due to the different structure of the dye. The influence of pH and ionic strength on the adsorption of the dye were analyzed. The pH study is presented in Figure 18a. With an increase in the solution pH, the amount of CR was less adsorbed for all samples. The highest value of adsorbent was obtained in a pH equal 4, where the attained amounts are about 14.4 mg g^{-1} for Fe_3O_4@1%Zn and 17.1 mg g^{-1} for Fe_3O_4@2%Zn. However, such a low pH is not recommended for the proposed nanoparticles due to their partial dissolution in acidic media below pH 4. At the pH 10, the amount was reduced to 4.2 mg g^{-1} for Fe_3O_4@10%Zn and 3.6 mg g^{-1} for Fe_3O_4@2%Zn, respectively. CR has anionic character [70], which is also similar to the TY case favorably adsorbed on a positively charged surface of an adsorbent, so acidic or neutral pH is better than alkalic for the effective removal of CR. Since the absorption efficiency was similar for all samples having different dopant content at pH 6, the following studies (ionic strength effect and isotherms) were performed at pH 6.

Next, complementary to TY studies, the effect of ionic strength on CR removal was also investigated at different concentrations of NaCl solution in a range from 0.04 mol dm^{-3} to 0.20 mol dm^{-3} concentration. In this case, we investigate this effect for Fe_3O_4@2%Zn and Fe_3O_4@10%Zn because we obtain the best results for these samples with CR. As shown in Figure 18b, for 0.04 concentration of salt, the amount of absorbency achieved is 11.8 mg g^{-1} for Fe_3O_4@2%Zn and 11.4 mg g^{-1} for Fe_3O_4@10%Zn. Increasing salt concentration to 0.20 mol dm^{-3}, the amount of absorbency achieved is 14.9 mg g^{-1} for Fe_3O_4@2%Zn but for Fe_3O_4@10%Zn it is only 12.1 mg g^{-1}.

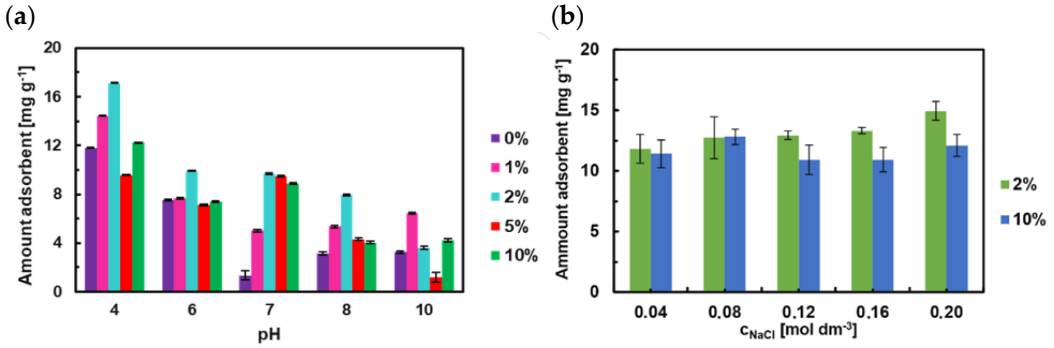

Figure 18. The (**a**) effect of pH and (**b**) the ionic strength on the adsorption of Congo red at pH 6.

4.4. Adsorption Isotherm for Congo Red

Complementary to the TY adsorption isotherms studies, measurements for CR were also performed, where analysis was made for the Fe_3O_4@10%Zn sample revealing the highest adsorption capacity. Figure 19 presents the experimental results and fitting to particular models.

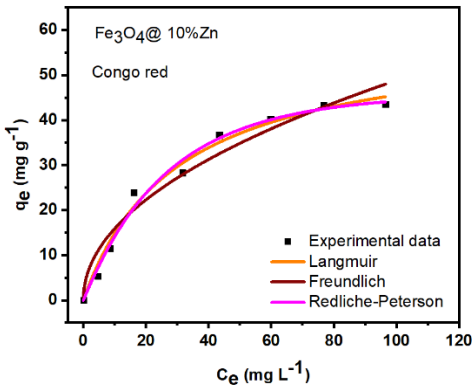

Figure 19. Isotherm modeling and experimental data for Fe_3O_4@10%Zn nanoparticles in pH equal 6.

Based on the isotherms' parameters as listed in Table 5, the R^2 adjusted and SD of Langmuir and Redlich-Peterson are relatively the same, which could imply that both isotherms are applicable for describing the adsorption of Congo red on Fe_3O_4@10%Zn. Meanwhile, the value of g in Redlich-Peterson as shown in Table 6 is 1.2. However, since the value of g must be less than 1, before it can be accepted to be suitable to describe the adsorption process, the best isotherm for the adsorption of Congo red using Fe_3O_4@10%Zn is Langmuir. This implies the monolayer adsorption of CR on the surface of Fe_3O_4@10%Zn. Table 7 shows the comparison of the experimental results obtained in this work for CR adsorption capacity with the literature.

Table 6. Adsorption parameters.

Fe_3O_4@10%Zn	
Langmuir	
$\boldsymbol{q_{max}}$ (mg g^{-1})	59
$\boldsymbol{K_L}$ (L mg^{-1})	0.033
$\mathbf{R^2_{adjusted}}$	0.984
SD (mg g^{-1})	2.07
Redlich-Peterson	
K_{RP} (L g^{-1})	1.64
a_{RP} (mg L^{-1})$^{-g}$	0.009
g	1.2
$\mathbf{R^2_{adjusted}}$	0.985
SD (mg g^{-1})	2.04
Freundlich	
$\boldsymbol{K_F}$ (mg g^{-1}) (mg L^{-1})$^{-1/nF}$	5.183
$\boldsymbol{n_F}$	2.06
$\mathbf{R^2_{adjusted}}$	0.945
SD (mg g^{-1})	3.75

Table 7. Comparison of the maximum adsorption (q_{max}) of different adsorbents for the removal of Congo red.

Adsorbents	**q_{max} (mg g^{-1})**	**References**
ZnO-polypyrrole magnetic nanocomposite	38.0	[71]
ZnO	25.0	[72]
magnetic HKUST-1	49.5	[73]
mesoporous-TiO_2/Fe_3O_4	50.0	[74]

Fe_3O_4	28.46	[75]
α-Fe_3O_4	57.2	[76]
SnO_2	24.27	[77]
Fe_3O_4@10%Zn	59.0	This work

4.5. Photocatalytic Studies for Congo Red

For Congo red, the highest photocatalytic efficiency is recorded for Fe_3O_4@10%Zn, see Figure 20 a–b. Based on TY research into photo-assisted degradation, Congo red dye used 20 mg of nanoparticles to 20 mL concentration 25-ppm model pollution. In the case of photocatalysis, Congo red achieved better results than Titan yellow. The highest % of removal was accomplished for 10% zinc dopped from 25 ppm to 7.1 ppm. After 60 min for Fe_3O_4 and Fe_3O_4@1%Zn and Fe_3O_4@5%Zn, the results are similar. Comparing photodegradation results, both dyes using Fe_3O_4@10%Zn removal are similar, at more than 70%. Fe_3O_4@2%Zn under UV-vis lamp obtains a higher percentage removal of CR than TY.

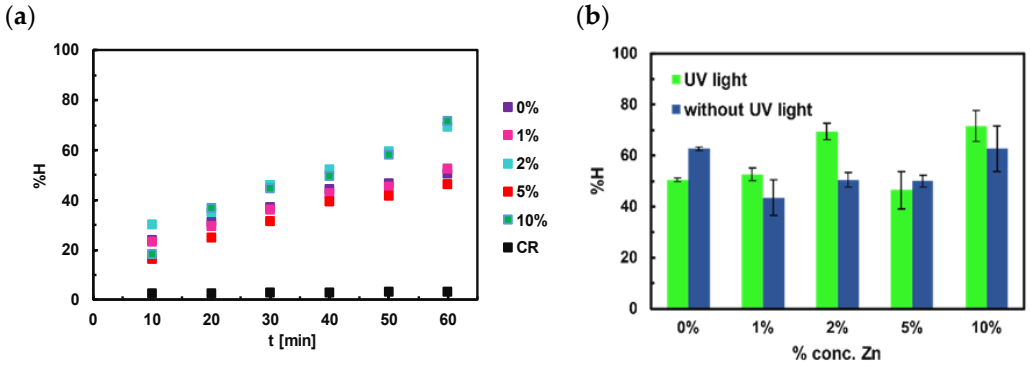

Figure 20. Efficiency of (**a**) photodegradation process by Fe_3O_4, Fe_3O_4@1%Zn, Fe_3O_4@2%Zn, Fe_3O_4@5%Zn, and Fe_3O_4@10%Zn nanoparticles after 60 min exposure time of Congo red and pristine dye, and (**b**) photo-assisted removal of CR in pH 6.

5. Conclusions

In this work, superparamagnetic iron oxide-based nanoparticles containing different levels of zinc dopant up to the 10% of the wt.% were synthesized and applied as an effective adsorbent of Titan yellow and Congo red sulphonic model dyes. The morphology of the prepared nanoparticles was estimated with SEM and TEM, revealing uniform round shape and size up to 15 nm. The increase of zinc content in the SPION structure improved their magnetization saturation, from 60.89 emu g^{-1} for pristine Fe_3O_4 to 68.72 emu g^{-1} for Fe_3O_4@10%Zn. A minor shift was observed in the diffractogram of the all the samples that contained Zn, which could be due to substitution of Fe with Zn. The BET studies show the total surface area is in the range of 85.7 to 101.5 m^2 g^{-1}, where the highest values were obtained for pristine Fe_3O_4 and Fe_3O_4@10%Zn. The amount of Titan yellow that was removed increased in line with an increase in the mass of the adsorbent, with the highest adsorption efficiency at 60 min of contact time. UV-vis studies also proved the highest adsorption efficiency for pristine Fe_3O_4 and Fe_3O_4@10%Zn for TY removal. The experimental data obtained using Fe_3O_4 fits well with the isotherm models as proposed by Langmuir, while that of Fe_3O_4@10%Zn was in accordance with the isotherm models proposed by Langmuir and Redlich-Peterson for TY. According to the Congo red adsorption process, Fe_3O_4@10%Zn could be fitted with the same models. The monolayer adsorption capacities for TY were 30 and 43 mg g^{-1} for Fe_3O_4 and Fe_3O_4@10%Zn towards TY treatment, respectively, and 59 mg g^{-1} Fe_3O_4@10%Zn for CR adsorption. These values are higher than some of the reported adsorbents in the literature for materials offering similar adsorption efficiency. It can be seen that even minor changes to the physicochemical properties of the proposed material have different effects on the adsorption efficiency and the photocatalytic degradation of dyes.

The main advantage of the proposed material is magnetic separation that enables the fast removal of sorbent from the solution without filtration and/or centrifuging. We show that direct dye treatment with a functional magnetic sorbent can be an easier solution and less energy-consuming than the photo-assisted method. The proposed material is effective in water pollutant treatment. However, there is a lack of commercial solutions for their management. The next step will include different dyes, including non-sulfonic molecules, their mixtures, and real wastewater treatment.

Author Contributions: Conceptualization, P.P. and M.O., Methodology, P.P., M.O.; Formal analysis, P.P., N.T.P., N.H.N.; Investigation, P.P., M.O., S.J.O.; Resources, M.O.; Data curation, P.P.; Writing—original draft preparation, P.P., M.O., S.J.O.; Writing—review and editing, all co-authors; Supervision, M.O., P.K.; Funding acquisition, D.T.M.T., M.G. All authors have read and agreed to the published version of the manuscript.

Funding: This research was partially funded by the Vietnam Academy of Science and Technology (VAST) with grant no. CT0000.09/21-23. Sunday J. Olusegun with No PPN/ULM/2020/1/00051/DEC/01, would like to thank the Polish National Agency for Academic Exchange (NAWA) for their support.

Institutional Review Board Statement: Not applicable.

Informed Consent Statement: Not applicable.

Data Availability Statement: Not applicable.

Acknowledgments: M.O. and N.T.P. would like to thank Ha Ngan Giang from the University of Science and Technology of Hanoi, Vietnam Academy of Science and Technology for technical support. M.O. and P.P. would like to thank Piotr Jenczyk from the Institute of Fundamental Technological Research, Polish Academy of Sciences for the SEM analyses support.

Conflicts of Interest: The authors declare no conflict of interest.

References

1. Maheshwari, K.; Agrawal, M.; Gupta, A.B. *Dye Pollution in Water and Wastewater*; In *Novel Materials for Dye-containing Wastewater Treatment. Sustainable Textiles: Production, Processing, Manufacturing & Chemistry*; Muthu, S.S., Khadir, A., Eds.; Springer: Singapore, **2021**, pp. 1–25. https://doi.org/10.1007/978-981-16-2892-4_1.
2. Lorenc-Grabowska, E.; Gryglewicz, G. Adsorption characteristics of Congo Red on coal-based mesoporous activated carbon. *Dye. Pigment.* **2007**, *74*, 34–40. https://doi.org/10.1016/j.dyepig.2006.01.027.
3. Le, P.T.; Bui, H.T.; Le, D.N.; Nguyen, T.H.; Pham, L.A.; Nguyen, H.N.; Nguyen, Q.S.; Nguyen, T.P.; Bich, N.T.; Duong, T.T.; et al. Preparation and Characterization of Biochar Derived from Agricultural By-Products for Dye Removal. *Adsorpt. Sci. Technol.* **2021**, *2021*, 14. https://doi.org/10.1155/2021/9161904.
4. Maru, K.; Kalla, S.; Jangir, R. Dye contaminated wastewater treatment through metal–organic framework (MOF) based materials. *New J. Chem.* **2022**, *46*, 3054–3072. https://doi.org/10.1039/D1NJ05015J.
5. Armağan, B.; Turan, M.; Çelik, M.S. Equilibrium studies on the adsorption of reactive azo dyes into zeolite. *Desalination* **2004**, *170*, 33–39. https://doi.org/10.1016/j.desal.2004.02.091.
6. Yang, X.; Wang, L.; Shao, X.; Tong, J.; Chen, R.; Yang, Q.; Yang, X.; Li, G.; Zimmerman, A.R.; Gao, B. Preparation of biosorbent for the removal of organic dyes from aqueous solution via one-step alkaline ball milling of hickory wood. *Bioresour. Technol.* **2022**, *348*, 126831. https://doi.org/10.1016/j.biortech.2022.126831.
7. Ayati, A.; Shahrak, M.N.; Tanhaei, B.; Sillanpää, M. Emerging adsorptive removal of azo dye by metal–organic frameworks. *Chemosphere* **2016**, *160*, 30–44. https://doi.org/10.1016/j.chemosphere.2016.06.065.
8. Elwakeel, K.Z.; Shahat, A.; Khan, Z.A.; Alshitari, W.; Guibal, E. Magnetic metal oxide-organic framework material for ultrasonic-assisted sorption of titan yellow and rose bengal from aqueous solutions. *Chem. Eng. J.* **2020**, *392*, 123635. https://doi.org/10.1016/j.cej.2019.123635.
9. Mishra, A.K.; Arockiadoss, T.; Ramaprabhu, S. Study of removal of azo dye by functionalized multi walled carbon nanotubes. *Chem. Eng. J.* **2010**, *162*, 1026–1034. https://doi.org/10.1016/j.cej.2010.07.014.
10. Hou, H.; Zhou, R.; Wu, P.; Wu, L. Removal of Congo red dye from aqueous solution with hydroxyapatite/chitosan composite. *Chem. Eng. J.* **2012**, *211–212*, 336-342. https://doi.org/10.1016/j.cej.2012.09.100.
11. Jiang, Y.; Gong, J.L.; Zeng, G.M.; Ou, X.M.; Chang, Y.N.; Deng, C.H.; Zhang, J. Liu, H.Y.; Huang, S.Y. Magnetic chitosan-graphene oxide composite for anti-microbial and dye removal applications. *Int. J. Biol. Macromol.* **2016**, *82*, 702-10. https://doi.org/10.1016/j.ijbiomac.2015.11.021
12. Nwaji, N.; Akinoglu, E.M.; Giersig, M. Gold Nanoparticle-Decorated Bi_2S_3 Nanorods and Nanoflowers for Photocatalytic Wastewater Treatment. *Catalysts* **2021**, *11*, 355. https://doi.org/10.3390/catal11030355.

13. Ghaemi, M.; Absalan, G.; Sheikhian, L. Adsorption characteristics of Titan yellow and Congo red on $CoFe_2O_4$ magnetic nanoparticles. *J. Iran. Chem. Soc.* **2014**, *11*, 1759–1766. https://doi.org/10.1007/s13738-014-0448-0.
14. Hou, X.; Feng, J.; Liu, X.; Ren, Y.; Fan, Z.; Wei, T.; Meng, J.; Zhang, M. Synthesis of 3D porous ferromagnetic NiFe2O4 and using as novel adsorbent to treat wastewater. *J Colloid Interface Sci.* **2011**, *15*,362(2), 477-85. https://doi.org/10.1016/j.jcis.2011.06.070
15. Tabaraki, R.; Sadeghinejad, N. Comparison of magnetic Fe_3O_4/chitosan and arginine-modified magnetic Fe_3O_4/chitosan nanoparticles in simultaneous multidye removal: Experimental design and multicomponent analysis. *Int. J. Biol. Macromol.* **2018**, *120*, 2313–2323. https://doi.org/10.1016/j.ijbiomac.2018.08.168.
16. Hu, L.; Guang, C.; Liu, Y.; Su, Z.; Gong, S.; Yao, Y.; Wang, Y. Adsorption behavior of dyes from an aqueous solution onto composite magnetic lignin adsorbent. *Chemosphere* **2020**, *246*, 125757. https://doi.org/10.1016/j.chemosphere.2019.125757.
17. Salem, M.A.; Salem, I.A.; Hanfy, M.G.; Zaki, A.B. Removal of titan yellow dye from aqueous solution by polyaniline/Fe_3O_4 nanocomposite. *Eur. Chem. Bull* **2016**, *5*, 113–118.
18. Ahmed, K.A.M. Formation Fe_2O_3 Nanowalls through Solvent-Assisted Hydrothermal Process and Their Application for Titan Yellow GR Dye Degradation. *J. Korean Chem. Soc.* **2014**, *58*, 205–209. https://doi.org/10.5012/JKCS.2014.58.2.205.
19. Akrami, A.; Niazi, A. Synthesis of maghemite nanoparticles and its application for removal of Titan yellow from aqueous solutions using full factorial design. *Desalin. Water Treat.* **2016**, *57*, 22618–22631. https://doi.org/10.1080/19443994.2015.1136693.
20. Brown, M.A.; De Vito, S.C. Predicting Azo Dye Toxicity. *Crit. Rev. Environ. Sci. Technol.* **1993**, *23*, 249–324. http://dx.doi.org/10.1080/10643389309388453.
21. Golka, K.; Kopps, S.; Myslak, Z.W. Carcinogenicity of azo colorants: Influence of solubility and bioavailability. *Toxicol. Lett.* **2004**, *151*, 203–210. https://doi.org/10.1016/j.toxlet.2003.11.016.
22. Hernández-Zamora, M.; Martínez-Jerónimo, F. Congo red dye diversely affects organisms of different trophic levels: A comparative study with microalgae, cladocerans, and zebrafish embryos. *Environ. Sci. Pollut. Res. Int.* **2019**, *26*, 11743–11755. https://doi.org/10.1007/s11356-019-04589-1.
23. Sharmila, M.; Mani, R.J.; Kader, S.M.A. Novel synthesis of undoped and zinc doped iron oxide nanoparticles using Apis Mellifera. *Mater. Today Proc.* **2022**, *50*, 2647–2649. https://doi.org/10.1016/j.matpr.2020.07.593.
24. Kiełbik, P.; Jończy, A.; Kaszewski, J.; Gralak, M.; Rosowska, J.; Sapierzyński, R.; Witkowski, B.; Wachnicki, Ł.; Lawniczak-Jablonska, K.; Kuzmiuk, P.; et al. Biodegradable Zinc Oxide Nanoparticles Doped with Iron as Carriers of Exogenous Iron in the Living Organism. *Pharmaceuticals* **2021**, *14*, 859. https://doi.org/10.3390/ph14090859.
25. Chen, F.; Bu, W.; Lu, C.; Chen, C.; Chen, M.; Shen, X.; Liu, R.; Shi, J. Hydrothermal synthesis of a highly sensitive T2-weigthed MRI contrast agent: Zinc-doped superparamagnetic iron oxide nanocrystals. *J. Nanosci. Nanotechnol.* **2011**, *11*, 10438–43. https://doi.org/10.1166/jnn.2011.3934.
26. Moise, S.; Céspedes, E.; Soukup, D.; Byrne, J.M.; El Haj, A.J.; Telling, N.D. The cellular magnetic response and biocompatibility of biogenic zinc- and cobalt-doped magnetite nanoparticles. *Sci. Rep.* **2017**, *7*, 39922. https://doi.org/10.1038/srep39922.
27. Paganini, M.C.; Giorgini, A.; Gonçalves, N.P.F.; Gionco, C.; Prevot, A.B.; Calza, P. New insight into zinc oxide doped with iron and its exploitation to pollutants abatement. *Catal. Today* **2019**, *328*, 230–234. https://doi.org/10.1016/j.cattod.2018.10.054.
28. Joseph, J.A.; Nair, S.B.; John, S.S.; Remillard, S.K.; Shaji, S.; Philip, R.R. Zinc-doped iron oxide nanostructures for enhanced photocatalytic and antimicrobial applications. *J. Appl. Electrochem.* **2021**, *51*, 521–538. https://doi.org/10.1007/s10800-020-01512-2.
29. Olusegun, S.J.; Mohallem, N.D.S. Comparative adsorption mechanism of doxycycline and Congo red using synthesized kaolinite supported CoFe2O4 nanoparticles. *Environ. Pollut.* **2020**, *260*, 114019. https://doi.org/10.1016/j.envpol.2020.114019.
30. Wang, J.; Yang, J.; Li, X.; Wang, D.; Wei, B.; Song, H.; Li, X.; Fu, S. Preparation and photocatalytic properties of magnetically reusable Fe_3O_4@ZnO core/shell nanoparticles. *Phys. E Low-Dimens. Syst. Nanostruct.* **2016**, *75*, 66–71. https://doi.org/10.1016/j.physe.2015.08.040.
31. Liu, J.; Zeng, M.; Yu, R. Surfactant-free synthesis of octahedral ZnO/$ZnFe_2O_4$ heterostructure with ultrahigh and selective adsorption capacity of malachite green. *Sci. Rep.* **2016**, *6*, 25074. https://doi.org/10.1038/srep25074.
32. Yang, C.; Florent, M.; de Falco, G.; Fan, H.; Bandosz, T.J. $ZnFe_2O_4$/activated carbon as a regenerable adsorbent for catalytic removal of H_2S from air at room temperature. *Chem. Eng. J.* **2020**, *394*, 124906. https://doi.org/10.1016/j.cej.2020.124906.
33. Yavuz, E.; Tokalıoğlu, Ş.; Patat, Ş. Magnetic dispersive solid phase extraction with graphene/$ZnFe_2O_4$ nanocomposite adsorbent for the sensitive determination of mercury in water and fish samples by cold vapor atomic absorption spectrometry. *Microchem. J.* **2018**, *142*, 85–93. https://doi.org/10.1016/j.microc.2018.06.019.
34. Wang, W.D.; Cui, Y.X.; Zhang, L.K.; Li, Y.M.; Sun, P.; Han, J.H. Synthesis of a novel $ZnFe_2O_4$/porous biochar magnetic composite for Th(IV) adsorption in aqueous solutions. *Int. J. Environ. Sci. Technol.* **2021**, *18*, 2733–2746. https://doi.org/10.1007/s13762-020-03023-1.
35. Olusegun, S.J.; Larrea, G.; Osial, M.; Jackowska, K.; Krysinski, P. Photocatalytic Degradation of Antibiotics by Superparamagnetic Iron Oxide Nanoparticles. Tetracycline Case. *Catalysts* **2021**, *11*, 1243. https://doi.org/10.3390/catal11101243.
36. Osial, M.; Rybicka, P.; Pękała, M.; Cichowicz, G.; Cyrański, M.K.; Krysiński, P. Easy Synthesis and Characterization of Holmium-Doped SPIONs. *Nanomaterials* **2018**, *8*, 430. https://doi.org/10.3390/nano8060430.
37. Nieciecka, D.; Celej, J.; Żuk, M.; Majkowska-Pilip, A.; Żelechowska-Matysiak, K.; Lis, A.; Osial, M. Hybrid System for Local Drug Delivery and Magnetic Hyperthermia Based on SPIONs Loaded with Doxorubicin and Epirubicin. *Pharmaceutics* **2021**, *13*, 480. https://doi.org/10.3390/pharmaceutics13040480.
38. Strobel, R.; Pratsinis, S.E. Direct synthesis of maghemite, magnetite and wustite nanoparticles by flame spray pyrolysis. *Adv. Powder Technol.* **2009**, *20*, 190–194. https://doi.org/10.1016/j.apt.2008.08.002.

39. Jozwiak, W.K.; Kaczmarek, E.; Maniecki, T.P.; Ignaczak, W.; Maniukiewicz, W. Reduction behavior of iron oxides in hydrogen and carbon monoxide atmospheres. *Appl. Catal. A Gen.* **2007**, *326*, 17–27. https://doi.org/10.1016/j.apcata.2007.03.021.
40. Amos-Tautua, B.M.; Fakayode, O.J.; Songca, S.P.; Oluwafemi, O.S. Effect of synthetic conditions on the crystallinity, porosity and magnetic properties of gluconic acid capped iron oxide nanoparticles. *Nano-Struct. Nano-Objects* **2020**, *23*, 100480. https://doi.org/10.1016/j.nanoso.2020.100480.
41. Demortière, A.; Panissod, P.; Pichon, B.P.; Pourroy, G.; Guillon, D.; Donnio, B.; Bégin-Colin, S. Size-dependent properties of magnetic iron oxidenanocrystals. *Nanoscale* **2011**, *3*, 225–232. https://doi.org/10.1039/C0NR00521E.
42. Saritha, A.; Raju, B.; Rao, D.N.; Roychowdhury, A.; Das, D.; Hussain, K.A. Facile green synthesis of iron oxide nanoparticles via solid-state thermolysis of a chiral, 3D anhydrous potassium tris(oxalato)ferrate(III) precursor. *Adv. Powder Technol.* **2015**, *26*, 349–354. https://doi.org/10.1016/j.apt.2014.11.005.
43. Anjana, P.M.; Bindhu, M.R.; Umadevi, M.; Rakhi, R.B.. Antimicrobial, electrochemical and photo catalytic activities of Zn doped Fe_3O_4 nanoparticles. *J Mater Sci: Mater Electron* **2018**, *29*, 6040–6050. https://doi.org/10.1007/s10854-018-8578-2
44. Nguyen, X.S..; Zhang, G..; Yang, X. Mesocrystalline Zn-Doped Fe_3O_4 Hollow Submicrospheres: Formation Mechanism and Enhanced Photo-Fenton Catalytic Performance. *ACS Appl. Mater. Interfaces.* **2017**, *9(10)*, 8900-8909. https://doi.org/10.1021/acsami.6b16839
45. Aghazadeh, M. Zn-doped magnetite nanoparticles: Development of novel preparation method and evaluation of magnetic and electrochemical capacitance performances. *J. Mater. Sci. Mater. Electron.* **2017**, *28*, 18755–18764. https://doi.org/10.1007/s10854-017-7824-3.
46. Paz-Díaz, B.; Vázquez-Olmos, A.R.; Almaguer-Flores, A.; García-Pérez, V.I.; Sato-Berrú, R.Y.; Almanza-Arjona, Y.C.; Garibay-Febles, V. $ZnFe_2O_4$ and $CuFe_2O_4$ Nanocrystals: Synthesis, Characterization, and Bactericidal Application. *J. Clust. Sci.* **2021**, *32*, 1-9. https://doi.org/10.1007/s10876-021-02203-4.
47. Shanmugavania, A.; Selvan, R.K. Synthesis of $ZnFe_2O_4$ nanoparticles and their asymmetric configuration with $Ni(OH)_2$ for a pseudocapacitor. *RSC Adv.* **2014**, *4*, 27022–27029.
48. Sun, S.; Yang, X.; Zhang, X.; Zhang, F.; Ding, J.; Bao, J.; Gao, C. Enhanced photocatalytic activity of sponge-like $ZnFe_2O_4$ synthesized by solution combustion method. *Prog. Nat. Sci. Mater. Int.* **2012**, *22*, 639–643. https://doi.org/10.1016/j.pnsc.2012.11.008.
49. Yao, J.; Yan, J.; Huang, Y.; Li, Y.; Xiao, S.; Xiao, J. Preparation of $ZnFe_2O_4/\alpha$-Fe_2O_3 Nanocomposites from Sulfuric Acid Leaching Liquor of Jarosite Residue and Their Application in Lithium-Ion Batteries. *Front. Chem.* **2018**, *6*, 422. https://doi.org/10.3389/fchem.2018.00442.
50. Briche, S.; Belaiche, M. Photocatalytic study of nanoferrites elaborated by sol-gel process for environmental applications. In Proceedings of the 2016 International Renewable and Sustainable Energy Conference (IRSEC), Marrakech, Morocco, 14–17 November **2016**; pp. 789–792. https://doi.org/10.1109/IRSEC.2016.7983986.
51. Fuentes-García, J.A.; Diaz-Cano, A.I.; Guillen-Cervantes, A.; Santoyo-Salazar, J. Magnetic domain interactions of Fe_3O_4 nanoparticles embedded in a SiO_2 matrix. *Sci. Rep.* **2018**, *8* (5096), 1-10. https://doi.org/10.1038/s41598-018-23460-w.
52. Sunil, K.C.; Utsav, S.; Nairy, R.K.; Chethan, G.; Shenoy, S.P.; Mustak, M.S.; Yerol, N. Synthesis and characterization of $Zn0.4Co0.6Fe_2O_4$ superparamagnetic nanoparticles as a promising agent against proliferation of colorectal cancer cells. *Ceram. Int.* **2021**, *47*, 19026–19035. https://doi.org/10.1016/J.CERAMINT.2021.03.248.
53. Correa-Duarte, M.A.; Grzelczak, M.; Salgueiriño-Maceira, V.; Giersig, M.; Liz-Marzán, L.M.; Farle, M.; Sierazdki, K.; Diaz, R. Alignment of Carbon Nanotubes under Low Magnetic Fields through Attachment of Magnetic Nanoparticles. *J. Phys. Chem. B* **2005**, *109*, 19060–19063. https://doi.org/10.1021/jp0544890.
54. Le, D.T.; Le, T.P.T.; Do, H.T.; Vo, H.T.; Pham, N.T.; Nguyen, T.T.; Cao, H.T.; Nguyen, P.T.; Dinh, T.M.T.; Le, H.V.; et al. Fabrication of Porous Hydroxyapatite Granules as an Effective Adsorbent for the Removal of Aqueous Pb(II) Ions. *J. Chem.* **2019**, *2019*, 8620181. https://doi.org/10.1155/2019/8620181.
55. Tran, H.N.; You, S.J.; Hosseini-Bandegharaei, A.; Chao, H.P. Mistakes and inconsistencies regarding adsorption of contaminants from aqueous solutions: A critical review. *Water Res.* **2017**, *120*, 88–116. https://doi.org/10.1016/j.watres.2017.04.014.
56. Lima, É.C.; Adebayo, M.A.; Fernando, M.M. Chapter 3—Kinetic and Equilibrium Models of Adsorption. In *Carbon Nanomaterials as Adsorbents for Environmental and Biological Applications*; Bergmann, C.P., Machado, F.M., Eds.; Springer: São Paulo, Brazil, **2015**; pp. 33–71. https://doi.org/10.1007/978-3-319-18875-1.
57. Bameri, I.; Saffari, J.; Baniyaghoob, S.; Ekrami-Kakhki, M.S. Synthesis of magnetic nano-$NiFe_2O_4$ with the assistance of ultrasound and its application for photocatalytic degradation of Titan Yellow: Kinetic and isotherm studies. *Colloids Interface Sci. Commun.* **2020**, *48*, 100610. https://doi.org/10.1016/j.colcom.2022.100610.
58. Shi, Q.X.; Li, Y.; Wang, L.; Wang, J.; Cao, Y.L. Preparation of supported chitosan adsorbent with high adsorption capacity for Titan Yellow removal. *Int. J. Biol. Macromol.* **2020**, *152*, 449–455. https://doi.org/10.1016/j.ijbiomac.2020.02.265.
59. Lakshmi, A.N.; Dhamodaran, M.; Samu Solomon, J. Thermodynamics and kinetics of adsorption of azo dye titan yellow from aqueous solutions on natural plant material Saccharum spontaneum. *Pharma Chem.* **2015**, *7*, 36–45.
60. Ibrahim, H.K.; Albo, M.A.; Allah, H.; Al-da, M.A. Adsorption of Titan Yellow Using Walnut Husks: Thermodynamics, Kinetics and Isotherm Studies. *Ann. Rom. Soc. Cell Biol.* **2021**, *25*, 12576–12587.
61. Okoronkwo, A.E.; Olusegun, S.J. Biosorption of nickel using unmodified and modified lignin extracted from agricultural waste. *Desalin. Water Treat.* **2013**, *51*, 1989–1997. https://doi.org/10.1080/19443994.2012.714896.

62. Vidya, C.; Manjunatha, C.; Sudeep, M.; Ashoka, S.; Lourdu Antony Raj, M.A. Photo-assisted mineralisation of titan yellow dye using ZnO nanorods synthesised via environmental benign route. *SN Appl. Sci.* **2020**, *2*, 743. https://doi.org/10.1007/s42452-020-2537-2.
63. Kooh, M.R.R.; Dahri, M.K.; Lim, L.B.L. The removal of rhodamine B dye from aqueous solution using Casuarina equisetifolia needles as adsorbent. *Cogent Environ. Sci.* **2016**, *2*, 1140553. https://doi.org/10.1080/23311843.2016.1140553.
64. Olusegun, S.J.; Mohallem, N.D.S. Insight into the adsorption of doxycycline hydrochloride on di ff erent thermally treated hierarchical $CoFe_2O_4$/bio-silica nanocomposite. *J. Environ. Chem. Eng.* **2019**, *7*, 103442. https://doi.org/10.1016/j.jece.2019.103442.
65. Samiey, B.; Ashoori, F. Adsorptive removal of methylene blue by agar: Effects of NaCl and ethanol. *Chem. Cent. J.* **2012**, *6*, 14. https://doi.org/10.1186/1752-153X-6-14.
66. Olusegun, S.J.; Freitas, E.T.F.; Lara, L.R.S.; Mohallem, N.D.S. Synergistic effect of a spinel ferrite on the adsorption capacity of nano bio-silica for the removal of methylene blue. *Environ. Technol.* **2021**, *42*, 2163–2176. https://doi.org/10.1080/09593330.2019.1694083.
67. Azazy, M.; Dimassi, S.N.; El-shafie, A.S.; Issa, A.A. Bio-Waste Aloe vera Leaves as an Efficient Adsorbent for Titan Yellow from Wastewater : Structuring of a Novel Adsorbent Using Plackett-Burman Factorial Design. *Appl. Sci.* **2019**, *9*, 4856. https://doi.org/10.3390/app9224856.
68. Raval, N.P.; Shah, P.U.; Shah, N.K. Adsorptive amputation of hazardous azo dye Congo red from wastewater: A critical review. *Environ. Sci. Pollut. Res.* **2016**, *23*, 14810–14853. https://doi.org/10.1007/s11356-016-6970-0.
69. Farrokhi, M.; Hosseini, S.C.; Yang, J.K.; Shirzad-Siboni, M. Application of ZnO–Fe3O4 Nanocomposite on the Removal of Azo Dye from Aqueous Solutions: Kinetics and Equilibrium Studies. *Water Air Soil Pollut* **2014**, *225*, 2113. https://doi.org/10.1007/s11270-014-2113-8.
70. Chakraborty, S.; Farida, J.J.; Simon, R.; Kasthuri, S.; Mary, N.L. Averrhoe carrambola fruit extract assisted green synthesis of zno nanoparticles for the photodegradation of congo red dye. *Surf. Interfaces* **2020**, *19*, 100488. https://doi.org/10.1016/j.surfin.2020.100488.
71. Karamipour, A.; Rasouli, N.; Movahedi, M.; Salavati, H. A Kinetic Study on Adsorption of Congo Red from Aqueous Solution by ZnOZnFe2O4-polypyrrole Magnetic Nanocomposite. *Phys. Chem. Res.* **2016**, *4*, 291–301. https://doi.org/10.22036/pcr.2016.14114.
72. Rath, P.P.; Behera, S.S.; Priyadarshini, B.; Panda, S.R.; Mandal, D.; Sahoo, T.; Mishra, S.; Sahoo, T.R.; Parhi, P.K. Influence of Mg doping on ZnO NPs for enhanced adsorption activity of Congo Red dye. *Appl. Surf. Sci.* **2019**, *491*, 256–266. https://doi.org/10.1016/j.apsusc.2019.06.120.
73. Xu, Y.; Jin, J.; Li, X.; Han, Y.; Meng, H.; Wang, T.; Zhang, X. Fabrication of hybrid magnetic HKUST-1 and its highly efficient adsorption performance for Congo red dye. *RSC Adv.* **2015**, *25*, 19199–19202. https://doi.org/10.1039/C5RA00384A.
74. Li, L.; Li, X.; Duan, H.; Wang, X.; Luo, C. Removal of Congo Red by magnetic mesoporous titanium dioxide–graphene oxide core–shell microspheres for water purification. *Dalton Trans.* **2014**, *43*, 8431–8438. https://doi.org/10.1039/C3DT53474J.
75. Mou, Y.; Yang, H.; Xu, Z. Morphology, Surface Layer Evolution, and Structure–Dye Adsorption Relationship of Porous Fe3O4 MNPs Prepared by Solvothermal/Gas Generation Process. *ACS Sustain. Chem. Eng.* **2017**, *5*, 2339–2349. https://doi.org/10.1021/acssuschemeng.6b02670.
76. Maiti, D.; Mukhopadhyay, S.; Devi, P.S. Evaluation of Mechanism on Selective, Rapid, and Superior Adsorption of Congo Red by Reusable Mesoporous α-Fe2O3 Nanorods. *ACS Sustain. Chem. Eng.* **2017**, *5*, 11255–11267. https://doi.org/10.1021/acssuschemeng.7b01684.
77. Said, M.; Rizki, W.T.; Asri, W.R.; Desnelli, D.; Rachmat, A.; Hariani, P.L. SnO_2–Fe_3O_4 nanocomposites for the photodegradation of the Congo red dye. *Heliyon* **2022**, *8*, E09204. https://doi.org/10.1016/j.heliyon.2022.e09204.